

351 CHAPTER 3

352 AMS-02 EXPERIMENT

353 3.1. Experiment Overview

354 The Alpha Magnetic Spectrometer (AMS) program was proposed by Nobel laureate Prof. Samuel
355 Ting from MIT in 1995 and was accepted then [74]. The goal of the experiment is to measure
356 the antimatter in cosmic rays and provide precise measurement of fluxes for different components of
357 cosmic rays, which is crucial to understanding the sources of cosmic rays and the basic propagation
358 model of cosmic rays. [75]

359 To test the feasibility of the particle spectrometer in space, a prototype called AMS-01 was designed,
360 a simplified version of the final experiment, see the detector in figure 3.1(a). The test flight was
361 conducted in 1998 in space shuttle flight STS-91 [76], see figure 3.1(b). By collecting cosmic rays
362 data for ten days, the test flight proved that putting a spectrometer in space is possible.

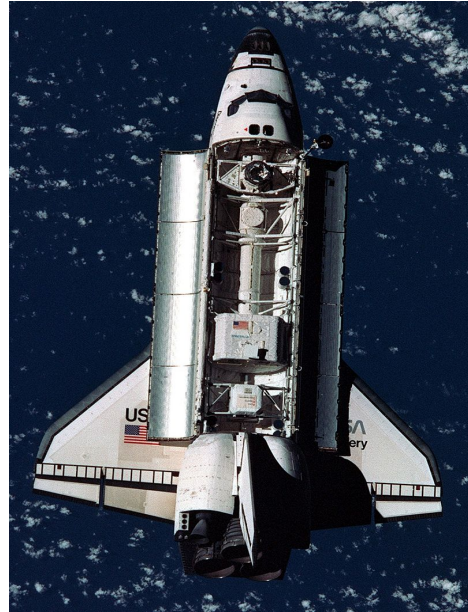
363 After several years of construction and testing, the AMS-02 detector was launched by space shuttle
364 Endeavour in STS 134 mission from Kennedy Space Center on 16 May 2011. Three days later, the
365 detectors were installed on ISS's upper Payload Attach Point (S3) and began data taking. Figure
366 3.2 shows the location of AMS-02 on the ISS.

367 The AMS-02 experiment has a size of $5\text{ m} \times 4\text{ m} \times 3\text{ m}$, weight of 7.5 t [80]. It has a permanent
368 magnet with 0.14 T, combined with nine silicon tracker layers, the rigidity of the particle can be
369 measured. Within the magnet, the Anti-Coincidence Counters (ACC) are used as a veto system to
370 reject particles from the side. At the relative top of the experiment, there is a Transition Radiation
371 Detector (TRD), which can distinguish light and heavy particles. Above and below the magnet
372 are two Time-Of-Flight (TOF) systems installed to provide the trigger and the measurements of
373 velocity and charge. Below the lower part of TOF, a Ring-Imaging Cherenkov (RICH) detector
374 is located so the particle's velocity can be measured. At the bottom of the detector, there is an
375 Electromagnetic Calorimeter (ECAL) which can measure the energy of particles. The geometry of
376 all the sub-detectors is illustrated in figure 3.3.

377 The experiment operations have been conducted since the launch to make the experiment run
378 smoothly. The operations can be split into flight and ground parts. For the flight part, the collected



(a)



(b)

Figure 3.1: a). AMS-01 test flight aboard Space Shuttle Discovery on the STS-91 mission in June 1998 [77] ; b). AMS-01 detector was installed in the support structure at Kennedy Space Center (NASA) [78] .



Figure 3.2: AMS-02 detector mounted on the ISS S3 Upper Inboard Payload Attach Site. Image modified from [79]

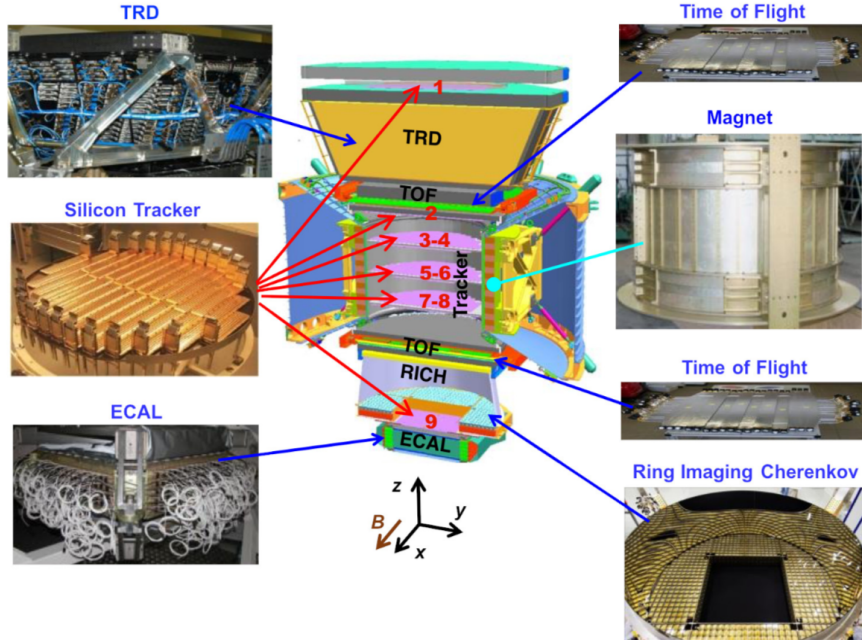


Figure 3.3: Schematic view of AMS-02 experiment and its all sub-detectors. [81]

379 data is transmitted from the ISS to tracking and data relay satellites (TDRS). Then through S and
 380 Ku band, the data is transmitted to white sands ground terminal (WSGT) in New Mexico. Over
 381 the NASA networks, the data is then directed to Marshall Space Flight Center (MSFC) and written
 382 on disk. At last, the data is copied to the payload operations control centre (POCC) at CERN.

383 3.2. Transition Radiation Detector

384 The TRD can separate different particles by transition radiations. Transition radiation is emitted
 385 when a charged particle goes through the boundary between two different media [82]. The
 386 emitted radiation is produced because of the different solutions of Maxwell's equation of charged
 387 particle in two media, so photons have to be emitted when particles cross the boundary. The
 388 intensity of emitted photon is proportional to the Lorentz factor γ , so for the relativistic charged
 389 particle, the characteristic energy of the radiation is X-ray. The direction is mostly forward, and the
 390 angle between transition radiation and particle path is proportional to $1/\gamma$.

391 AMS-02 experiment has a transition radiation detector placed on the top of the experiment between
 392 tracker layer one and the upper TOF layer [83, 84]. The TRD has 5248 proportional tubes; each
 393 one has a 6 mm diameter and a maximum of 2 meters in length. The tubes have double-layer 72 μm
 394 Kapton aluminum foil walls and at the center of the tube is 30 μm tungsten wire. Inside the tubes
 395 there are CO₂ and Xe gas mixture supplied from storage tanks (5 kg CO₂ and 49 kg Xe). When a
 396 charged particle goes through the tube, it can ionize the Xe atom and a high voltage is produced
 397 on the wire. After that, it creates an avalanche of ionization proportional to the charged particle's
 398 energy loss. Then the CO₂ could quench the environment and reset to the initial state. So far, no



Figure 3.4: The construction of the TRD. [85]

399 detectable leak in the AMS-02 TRD gas system has been observed. Due to the diffusion, the loss
 400 of CO₂ is around 0.47 g/day, and the loss is ignorable for Xe. This ensures that TRD can stably
 401 operate until 2035.

402 These TRD tubes are assembled in 328 modules, and one module has 16 tubes. Furthermore, all
 403 these modules are mounted in 20 layers. Twelve layers are placed along the Y axis in the middle of
 404 TRD, four layers are placed on top, and four layers are on the bottom. In figure 3.4, the actual size
 405 of TRD is shown.

406 In figure 3.5, the left figure shows the response when an electron and a proton go through one TRD
 407 layer. The upper part of the layer is a 20 mm fleece radiator, which has 10 μm polypropylene or
 408 polyethylene fibers. The lower part of the layer is straw tubes. When a relativistic charged particle
 409 goes through the radiator, transition radiation may be produced. For example, the dE/dx signal
 410 can be recorded after a proton traverses the layer. While an electron passes the layer, the transition
 411 radiation can also be collected in straw tubes. The right figure shows the distributions in tube
 412 collected energy for 100 GeV protons and 20 GeV electrons as an example. Due to the transition
 413 radiation emitted by electrons, around 10 keV photons are observed.

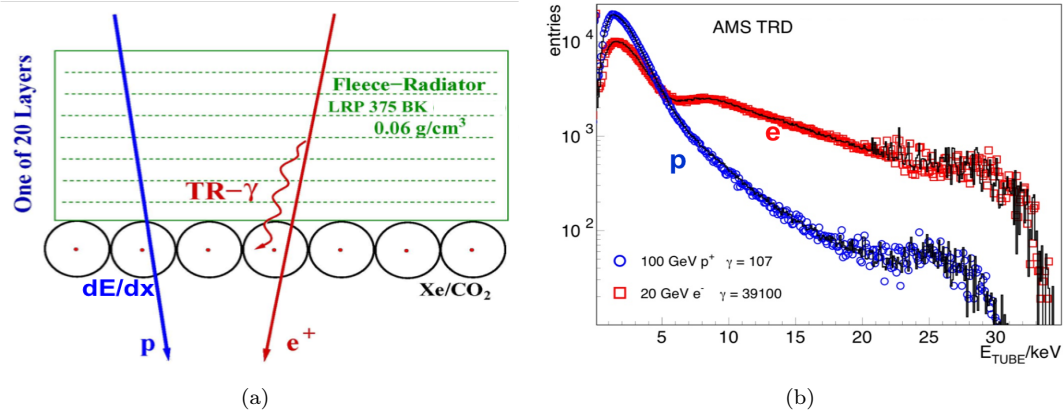


Figure 3.5: Illustration of TRD separation between electrons and protons [85] : the left figure shows the transition radiation emitted by positron while proton only left dE/dX signal; the right figure shows an example of tube collected energy for 100 GeV protons and 20 GeV electrons

414 3.3. Silicon Tracker

415 To measure the rigidity and its sign, a silicon tracker system with a magnet is equipped in the
 416 AMS-02 experiment. The magnet used in the AMS-02 experiment is a permanent magnet with a
 417 0.14 T magnetic field. The magnet has 64 Nd-Fe-B sectors arranged in a cylinder shape with 0.8 m
 418 height and 1.1 m diameter inside. The produced magnetic field is almost linear, and the magnetic
 419 field direction is defined as the X direction, the vertical direction is the Z direction, so the particle
 420 bending plane is the YZ plane. Outside the magnet, the leaking magnetic field is ignorable so that
 421 the design can minimize the magnetic effect on the ISS. In figure 3.6, the permanent magnet used
 422 in AMS-02 is shown.

423 The tracker in AMS-02 has nine silicon layers, the first layer is on the top of TRD, the second layer is
 424 above the magnet and below the upper TOF, and layer 3 to 8 are inner central layers installed inside
 425 the permanent magnet, layer 9 is above ECAL and below RICH. In figure 3.7, a tracker inner plane
 426 equipped with ladders is shown. In total, all nine layers have 2264 double-sided silicon micro-strip
 427 sensors. They are arranged into 192 ladders [86, 87]. The summed-up active measurement area is
 428 6.75 m^2 . Each ladder has 1024 readout strips for signal readout, 640 on the p-side and 384 on the
 429 n-side. So in total, 196608 readout strips are reading out the signals.

430 The double-sided silicon micro-strip sensor has size of $41.360 \times 72.045 \text{ mm}^2 \times 300 \mu\text{m}$. A particle
 431 goes through the sensor and creates electron-hole pairs in the middle. The created electrons drift
 432 toward the n-side and the holes toward the p-side, the X position measurement is obtained from
 433 n-side and the Y position measurement is obtained from p-side. Figure 3.8 illustrate the process.
 434 The tracker's design results in resolutions of $10 \mu\text{m}$ and $30 \mu\text{m}$ in bending direction and non-
 435 bending direction respectively for protons. By giving the hit position, the rigidity and its sign can
 436 be reconstructed.

437 According to the existence of tracker track hits in different layers, the different categories of tracker



Figure 3.6: Preparing for the vibration test of the permanent magnet in China Academy of Launch Vehicle Technology (CALT) [85]

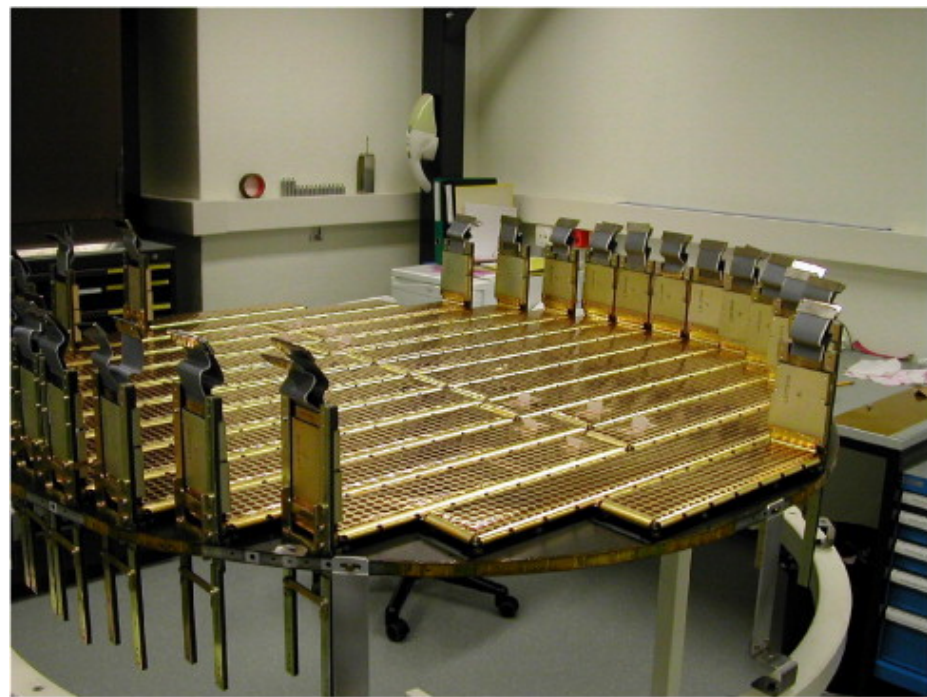


Figure 3.7: A silicon tracker inner plane fully equipped with shielded ladders. [88]

438 patterns can be defined. In table 3.1, all the tracker pattern definitions are given. In this table,
439 ✓ denotes "have a hit associated to the track in this layer" and × denotes "does not have a hit
440 associated to the track in this layer".

Table 3.1: Table of tracker pattern definitions.

Tracker Pattern	Layer 1	Layer 2	Layer 9
0	✓	✓ or ×	✓
1	✓	✓	✗
2	✗	✓	✓
3	✓	✗	✗
4	✗	✓	✗
5	✗	✗	✓
-1	✗	✗	✗

441 In addition, the deposited ionization energy dE/dX is proportional to the square of the particle
442 charge Z^2 . Therefore, the charge measurement of each layer can be obtained. The charge resolution
443 of the inner tracker layers is $\Delta Z = 0.05$ for the charge one particle.

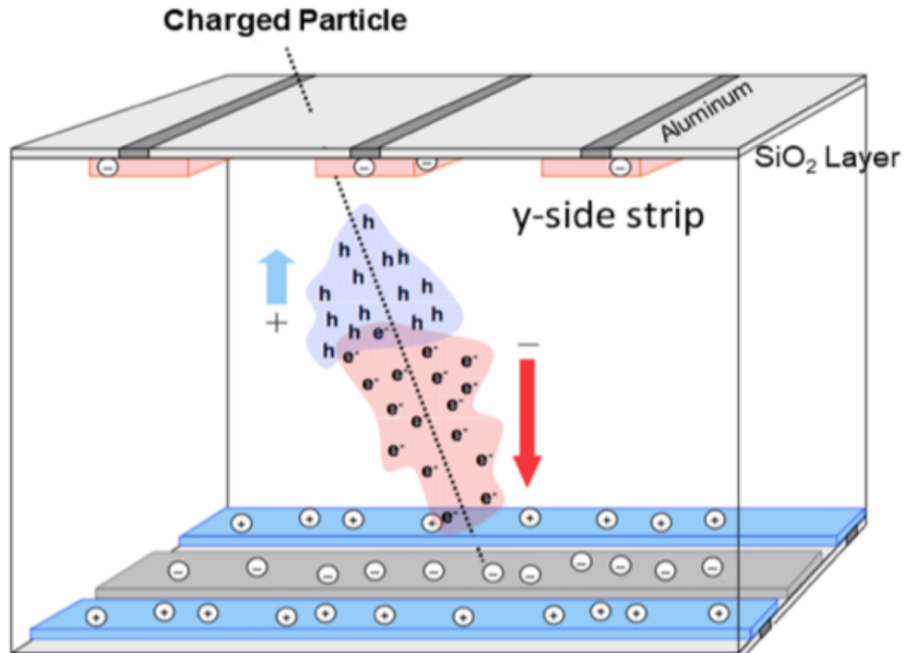


Figure 3.8: Drift of the electron-hole pair in silicon sensor produced by a charged particle. [85]

444 The inner tracker layer's positions are aligned with 20 IR laser beams with sub-micron measurement
445 [89, 90]. Layer 1 and 9 position alignments are done with 2 minutes cosmic rays. This gives 5 μm
446 and 6 μm variations for layer 1 and 9, respectively.

447 Before the launch of AMS-02, the whole detector was tested at CERN SPS with proton beams of 180
448 and 400 GeV, positron, electron, and pion beams of 10 to 290 GeV. These extensive calibration data

449 give precise measurement to determine the tracker rigidity resolution function and make it possible
450 to compare and calibrate with MC simulation. Figure 3.9 shows the 400 GeV proton calibration
451 data and MC comparison. A good match between these two is seen.

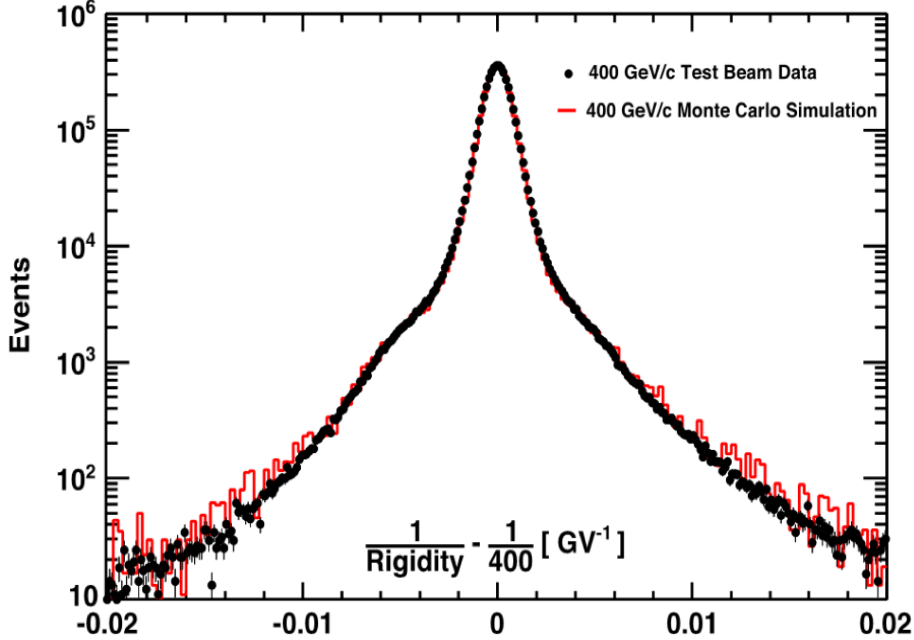


Figure 3.9: Tracker resolution comparison between 400 GeV protons beam test and MC comparison.
[85]

452 Due to the resolution of the tracker and the multiple scattering [91], the resolution of the momentum
453 measurement can be described by:

$$\left(\frac{\sigma_p}{p}\right)^2 = \left(\sqrt{\frac{720}{N+4}} \frac{\sigma_x p \sin \theta}{0.3BL^2}\right)^2 + \left(\frac{0.2}{\beta B \sqrt{LX_0} \sin \theta}\right)^2 \quad (3.1)$$

454 where p is the momentum of the charged particle, B is the magnetic field, N is the equidistant
455 measurements, θ is the track inclination angle, L is the track length in the bending plane, σ_x is the
456 sagitta resolution in the bending plane, $\beta = \frac{v}{c}$, X_0 is the radiation length of the traversed medium,
457 σ_x is the sagitta resolution in the bending plane.

458 In this equation, the momentum measurement is determined by two parts. The first term is the
459 contribution of tracker resolution and the second term is the contribution of multiple scattering.
460 Since $R = pc/Ze$, the rigidity resolution is obtained. The AMS-02 tracker resolution has been
461 studied extensively. In figure 3.10, the rigidity resolution for proton is shown. Below 1.5 GV,
462 the rise is due to the multiple scattering, and the rise in the high rigidity range is mostly due to
463 resolution. The maximum detectable rigidity (MDR) is defined as the $\sigma_R = R$ and this value is
464 usually used to describe the highest rigidity can be measured. For AMS-02 tracker, the MDR for

⁴⁶⁵ proton in full span (tracker pattern 0) is around 2 TV.

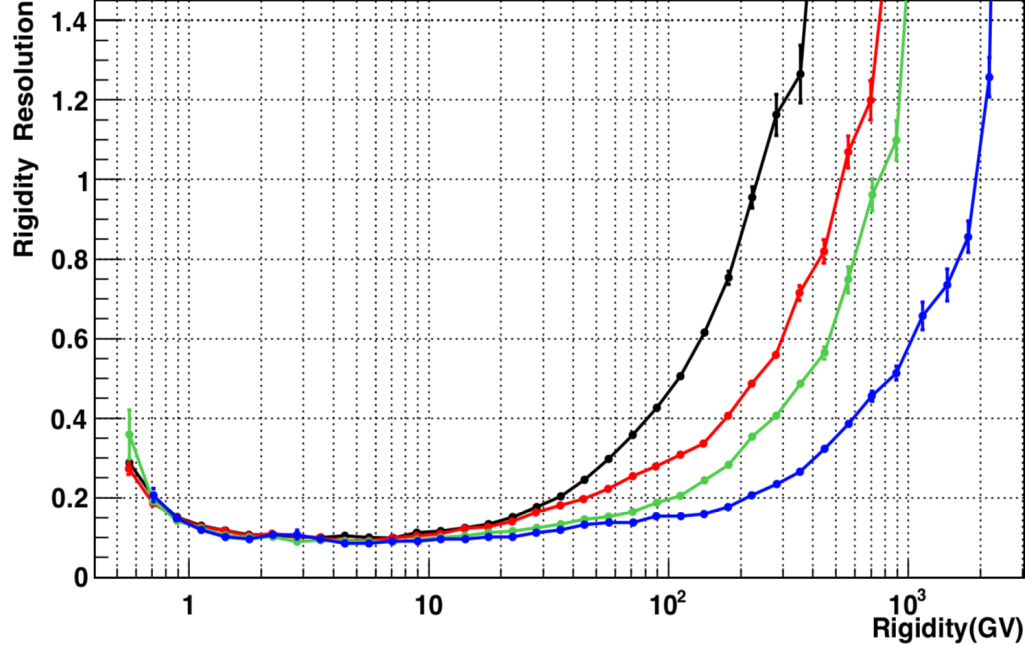


Figure 3.10: Tracker resolution from MC simulation for proton [92]. The four curves are in different tracker patterns: Black for inner tracker only, red for inner tracker plus layer 1, green for inner tracker plus layer 9, blue for inner tracker plus layer 1 and 9.

⁴⁶⁶ 3.4. Time Of Flight

⁴⁶⁷ AMS-02 has four planes of TOF counters, plane 1 and 2 are above the magnet (Upper TOF), and
⁴⁶⁸ plane 3 and 4 are below the magnet (Lower TOF) [93, 94]. Plane 1, 2, and 4 have eight plastic
⁴⁶⁹ scintillator paddles, while plane 3 has ten paddles. The paddles have different lengths between 117
⁴⁷⁰ and 134 cm and a thickness of 1 cm. In upper and lower TOF, two planes are arranged in X and
⁴⁷¹ Y directions, respectively, see figure 3.11. To avoid possible gaps between paddles, the paddles are
⁴⁷² placed with a 0.5 cm overlapping. Each paddle is also equipped with 2 or 3 PMTs at the end of the
⁴⁷³ paddle, so the light signal from the plastic scintillator paddle can be collected by these PMTs and
⁴⁷⁴ provide efficient detections.

⁴⁷⁵ Combining the information from all four planes, the TOF system can provide the particle triggers
⁴⁷⁶ for the AMS-02 experiment. More details about triggers will be discussed in 4.7.

⁴⁷⁷ TOF can get the particle's velocity by measuring the time differences between upper and lower TOF.
⁴⁷⁸ Each counter's time resolution is around 160 ps, and the combined β resolution is around 4% for
⁴⁷⁹ $\beta \approx 1$ and $Z = 1$ particles. See figure 3.12(a). This provides the ability to discriminate between the
⁴⁸⁰ up-going and down-going particles.

⁴⁸¹ Except for measuring the velocity, TOF can also get the particle's charge. By measuring the ioniza-

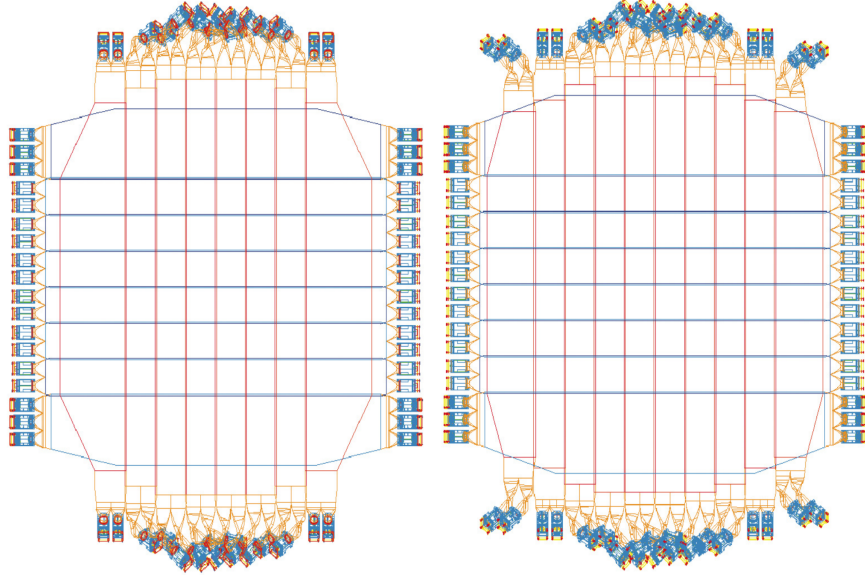


Figure 3.11: TOF planes arrangement in AMS-02 experiment, left is Upper TOF and right is Lower TOF [95].

tion energy loss dE/dX , the charge of particles can be independently obtained from the anode and dynode of PMTs. See figure 3.12(b). The charge resolution is $\Delta Z = 0.05$ for the charge one particle.

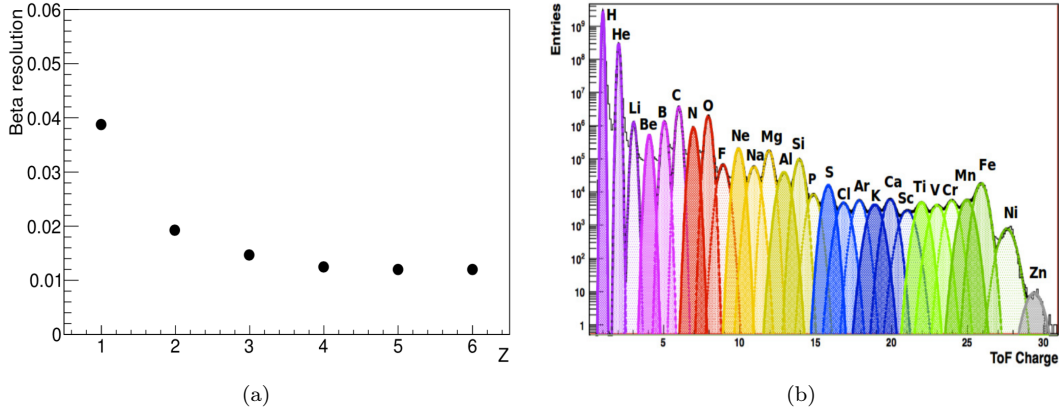


Figure 3.12: a). TOF Beta resolution as the function for particle charge. [95] ; b). TOF charge distribution from proton ($Z=1$) to Zinc ($Z=30$). [95]

484 3.5. Ring-Imaging Cherenkov Detector

In the AMS-02 experiment, the RICH is installed below the lower TOF and above ECAL. The RICH can measure the velocity and the charge of relativistic particles. It has two radiators at the top, NaF radiator at the center and AgI radiator as the outer radiator. Below the two radiators, there is an expansion volume in the middle, and a PMT plane at the bottom [96, 97]. In figure 3.13, the

489 components of the RICH are shown. The whole RICH has the shape of a cone with an upper radius
490 of 60 cm, a lower radius of 67 cm, and a height of 47 cm.

491 When a charged particle traverses a dielectric radiator with a velocity greater than the velocity of
492 light in this material, the particle emits a cone of Cherenkov photons. By measuring the emission
493 opening angle of the Cherenkov radiation cone $\theta = \arccos(1/n\beta)$, the β of the particle can be ob-
494 tained. The RICH in the AMS-02 experiment has a radiator plane of two non-overlapping radiators.
495 The central radiator has 16 sodium fluoride tiles (NaF) of $85 \times 85 \times 5\text{mm}^3$ with refractive index
496 $n=1.33$. Outside of NaF, there are 92 silica aerogel tiles (Agl) of $115 \times 115 \times 25\text{mm}^3$ with refractive
497 index $n=1.05$ [96].

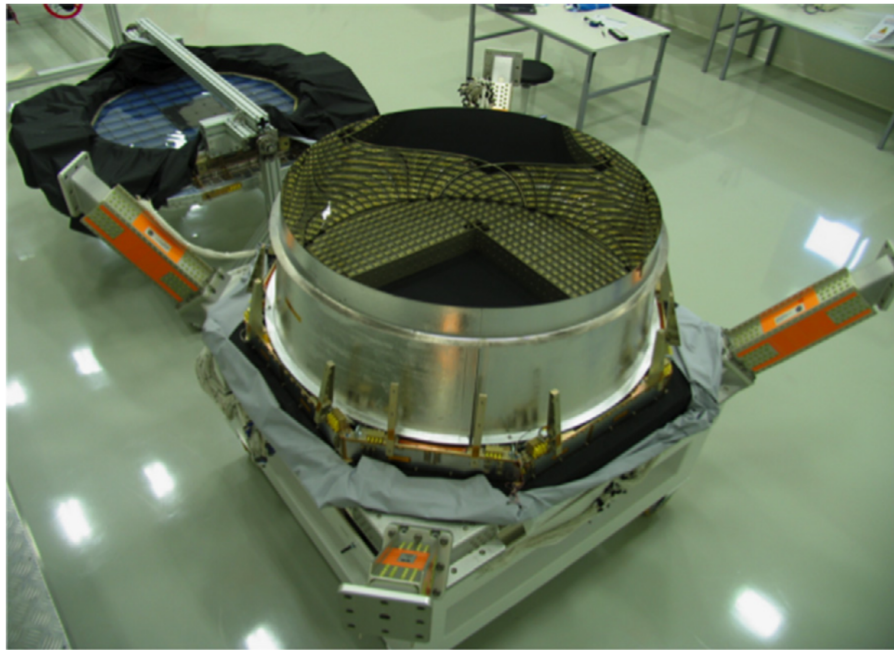


Figure 3.13: RICH PMT plane and expansion volume in the front and two radiators in the behind.
[98]

498 Since $\beta = v/c$ and $n = c/v$, this leads to the requirement that particles of $\beta > 0.75$ for NaF and
499 particles of $\beta > 0.953$ for Agl can emit radiation.

500 A highly reflective mirror surrounds the expansion volume to increase the detection efficiency. The
501 PMT detection plane at the bottom is equipped with 680 PMT tubes of 4×4 multi anodes. These
502 PMTs detect the Cherenkov photons emitted in the radiators, and the effective spatial granularity
503 is $8.5 \times 8.5\text{mm}^2$. Since the sum of the signal amplitudes is proportional to Z^2 , the charge of the
504 particle can also be measured.

505 The velocity resolution of RICH is $\sigma_\beta/\beta \approx 10^{-3}$ for charge one particle with the aerogel radiator, see
506 figure 3.14(a). The charge measurement of RICH provides a resolution better than 0.5 for particles
507 of charge up to 12, see figure 3.14(b) for the resolutions.

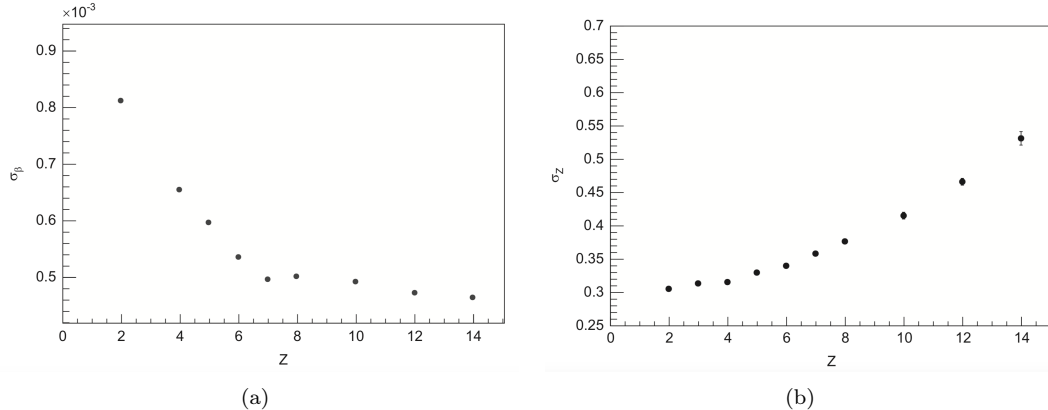


Figure 3.14: a). RICH beta resolution as the function for particle charge with the aerogel radiator. [99] ; b). RICH charge resolution as the function of particle charge. [99]

508 3.6. Electromagnetic Calorimeter

509 The ECAL in the AMS-02 experiment can precisely measure the longitudinal and lateral electro-
 510 magnetic shower development and also the deposited energy [100, 101]. It has a lead-scintillating
 511 fiber sandwich structure with an active area of $648 \times 648\text{mm}^2$, a thickness of 166mm and a weight
 512 of ≈ 500 kg. The ECAL has 98 lead foils and 50000 scintillating fibers in total. The entire structure
 513 corresponds to 17 radiation lengths for a total depth.

514 The ECAL consists of 9 superlayers with a thickness of 18.5 mm. Each superlayer is made of 11
 515 grooved lead foils alternate with ten fiber layers glued together with optical epoxy (see figure 3.16)
 516 [102], while the last superlayer is made of aluminum. Also, one superlayer is placed in one direction
 517 only. By alternatively stacking the nine superlayers in X and Y directions, the 3D image of the
 518 shower shape is obtained (five in the X direction and four in the Y direction). Each superlayer is
 519 read out by 36 PMTs at only one edge. To avoid dead zone, the PMTs are arranged alternatively.
 520 In total, the ECAL has 324 PMTs. [103].

521 When a particle goes through the ECAL, it will interact in an electromagnetic or a hadronic way
 522 to produce a shower [104]. When an electron or positron traverses the ECAL, it emits photons
 523 by bremsstrahlung, then the emitted photons convert to electrons and positrons further by pair
 524 production, so the cascaded electromagnetic shower develops and is shaped. While a proton or
 525 antiproton traverses the ECAL, it passes as a minimum ionizing particle (MIP) and leaves a relatively
 526 clear track. The nearby hadronic shower primarily consists of pions and kaons by interaction or decay.
 527 Due to the transverse momenta for massive secondaries and the possible production of neutral
 528 particles, the hadronic shower looks wider and more likely to be irregular than the electromagnetic
 529 shower.

530 The different shower shapes can be used to distinguish electrons and protons (antiprotons). Com-
 531 bined with the Tracker measurement ($E/|R|$ cut), the ECAL provides a proton rejection power of
 532 above 10^4 from 3 GeV to 1000 GeV at an electron efficiency of 90%. In figure 3.15, the rejection

533 power of ECAL is shown.

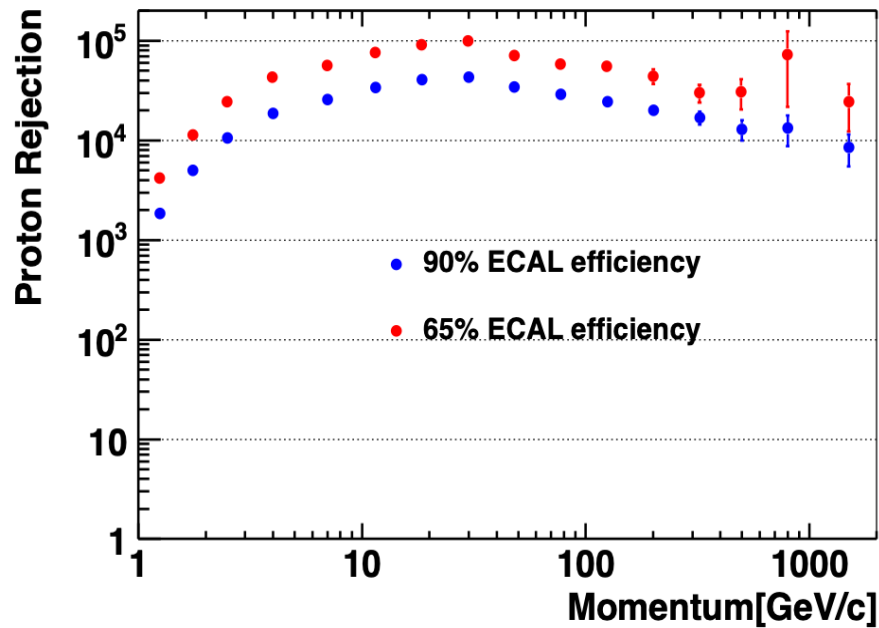


Figure 3.15: Proton rejection power of ECAL at 65% and 90% electron efficiency. [85]

534 The energy resolution has been determined by beam test [105] and can be described by [106] :

$$\frac{\sigma(E)}{E} = \frac{(10.4 \pm 0.2)\%}{\sqrt{E(\text{GeV})}} \oplus (1.4 \pm 0.1)\% \quad (3.2)$$

535 In figure 3.17, the comparison between measured data and the function is given.

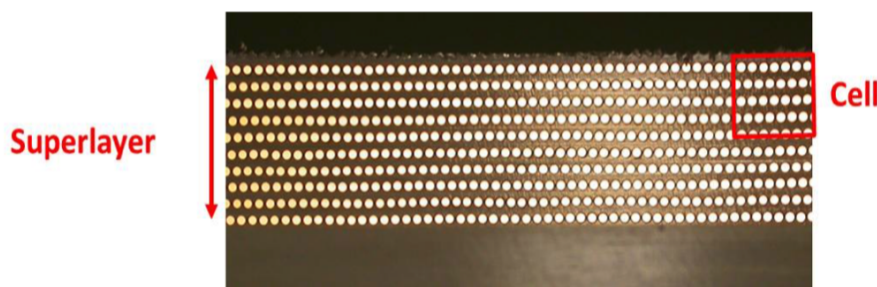


Figure 3.16: ECAL super layer structure and cell dimensions. [103]

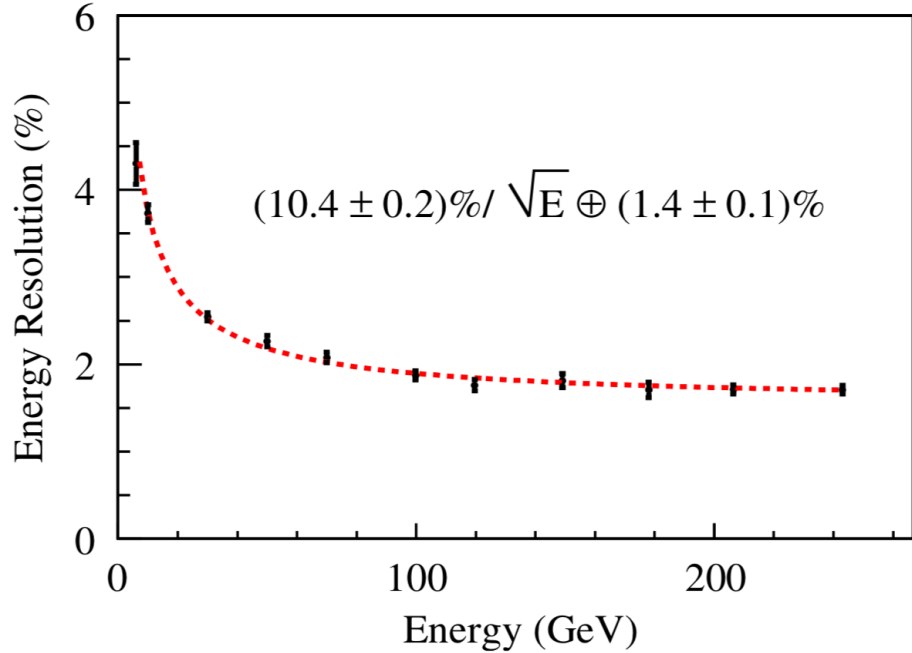


Figure 3.17: ECAL energy resolution from beam test data [106].

536 3.7. Anti-Coincidence Counter

537 The ACC in the AMS-02 experiment is installed surrounding the inner tracker inside the magnet bore
 538 [107, 108], see figure 3.18 upper left one. The first purpose is to reject unwanted events like particles
 539 entering the AMS-02 from the side, back-scattering from the ECAL, or secondary interacting with
 540 the sub-detectors. The second task for the ACC is to reduce the trigger rate when the ISS is going
 541 through the area overwhelmingly dominant by low energy large flux like SAA [109].

542 The ACC has a cylinder shape of 1.1 m in diameter and 0.83 m in height. It is composed of 16
 543 scintillator panels (Bicron BC-414) with 8 mm thickness, see the upper right figure in 3.18. When
 544 the particles traverse the ACC panels, the particle will emit photons by ionization energy loss in the
 545 scintillators. Then the light would be absorbed by the fibers (WLS, Kuraray Y-11(200)M) that are
 546 embedded into the panels, and transported to PMTs (Hamamatsu R5946) at the end.

547 A pair of panels are connected to two same PMTs through clear fibers, see figure 3.18 lower one. The
 548 design is to have redundancies and also save weight. The slot between these two panels has a tongue
 549 and groove structure to minimize the inefficiency of detections. After integrating sub-detectors in
 550 2008, panels' efficiency is determined at CERN using muons to be 99.99% [85].

551 By cutting on the ACC scintillators fired during the event, the ACC system is used to veto particles
 552 crossing from the side of the detector. Combined with the information from the TOF, the level 1
 553 trigger is generated to acquire the event. More detail about the ACC's role in trigger will be given
 554 in section 4.7.

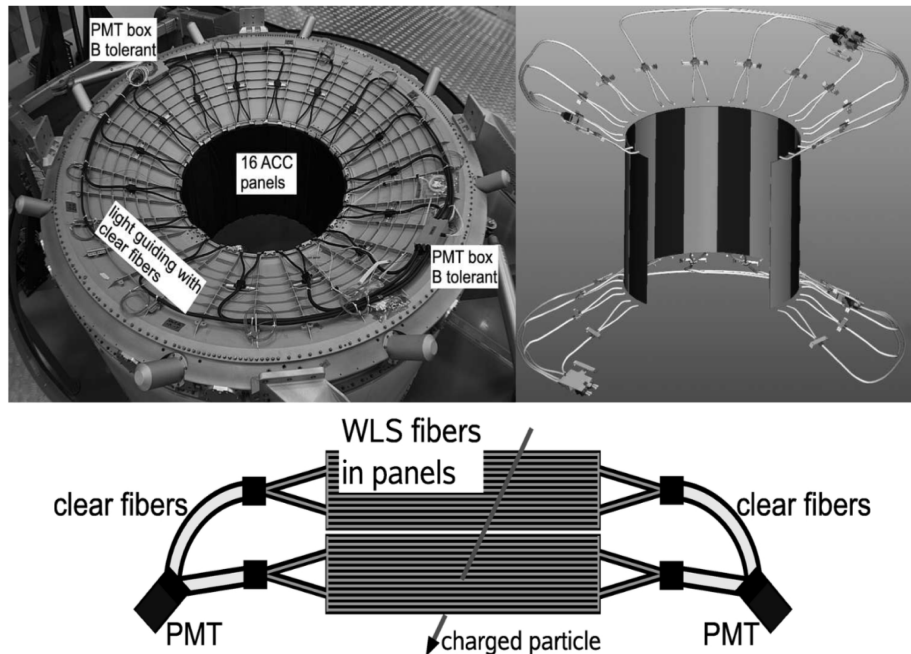


Figure 3.18: Upper left: ACC counter system. Upper right: the principle of ACC arrangement. Lower: Panel pair and PMTs connections. [110]

1237 APPENDIX

1238 Input variables for charge confusion

1239 Except for the four variables shown in section 4.2, the full list of the 12 left input variables used
1240 in the training charge confusion estimator is given in this appendix. Nine of them are constructed
1241 from the Tracker, two of them are constructed from the TOF, and one of them is constructed from
1242 the TRD.

1243 1. TOF Charge

1244 For the TOF subdetector, the charge measurements are used in training. **UpperTofCharge**
1245 and **LowerTofCharge** are the TOF charge measurements from upper TOF and lower TOF.
1246 In figure 1, the distributions of the **UpperTofCharge** and **LowerTofCharge** are shown.

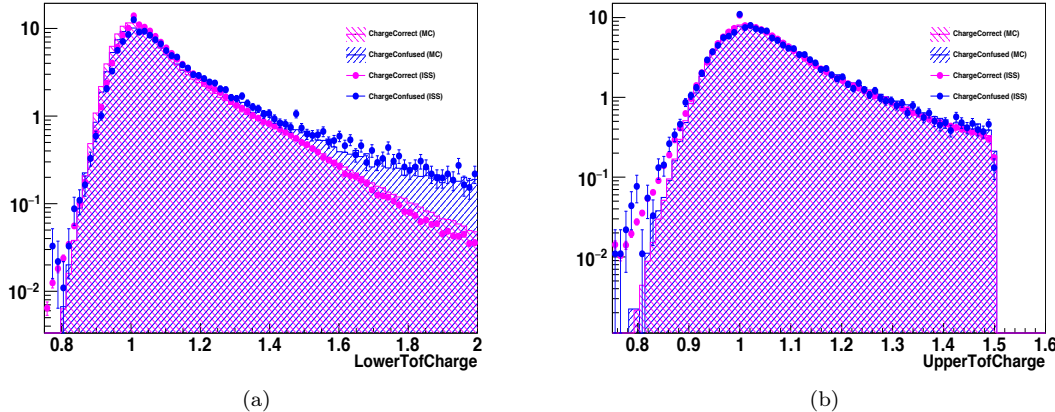


Figure 1: Distributions of a). **LowerTofCharge** b). **UpperTofCharge** in example rigidity bin of 330 to 525 GV. Histograms (magenta: charge correct; blue: charge confused) are taken from MC and points (magenta: charge correct; blue: charge confused) are from data.

1247 2. Rigidity Asymmetry and Matching

1248 The rigidity is constructed from the Tracker. With the different tracker layers, different rigidity
 1249 values are obtained. Therefore, the asymmetry and matching variables can be constructed
 1250 further and used as the inputs of training. Two variables related to this are used: **Rigid-
 1251 ityAsymmetryL9** and **InnerRigidityMatch**. The definitions are given below:

$$\text{RigidityAsymmetryL9} = \frac{\text{RigidityInnerL9} - \text{RigidityInner}}{\text{RigidityInnerL9} + \text{RigidityInner}}$$

$$\text{InnerRigidityMatch} = \left[\left(\frac{1.0}{\text{RigidityInnerUpper}} \right) - \left(\frac{1.0}{\text{RigidityInnerLower}} \right) \right] \cdot \frac{100 \cdot R}{|R|}$$

1252 where the RigidityInner and RigidityInnerL9 are the rigidities constructed from the inner
 1253 tracker layer and the inner tracker layer plus layer 9, RigidityInnerUpper and RigidityInner-
 1254 Lower are constructed from the upper half of the inner tracker layer and the lower half of the
 1255 inner tracker layer.

1256 In figure 2, the distributions of the two variables are shown.

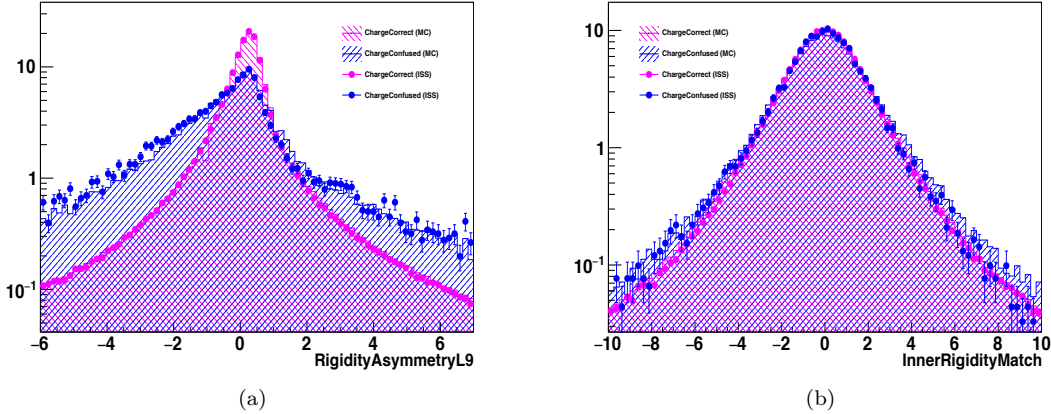


Figure 2: Distributions of a). **RigidityAsymmetryL9** b). **InnerRigidityMatch** in example rigidity bin of 330 to 525 GV. Histograms (magenta: charge correct; blue: charge confused) are taken from MC and points (magenta: charge correct; blue: charge confused) are from data.

3. Tracker Fit Chi2

The tracker track fit quality provides important information for charge confusion. Due to the interaction, the poorer fit quality is, the more likely the event to be charge confused. Therefore, the fit Chi2 could be used as the input for training. In total, four variables related to Chi2 are used: **TrackerChi2X** and **TrackerChi2Y** are the tracker track fit Chi2 in logarithmic on X and Y sides respectively. **InnerTrackerChi2X** and **InnerTrackerChi2Y** are the inner tracker track fit Chi2 in logarithmic on X and Y sides respectively. In figure 3, the distributions of these four variables are shown.

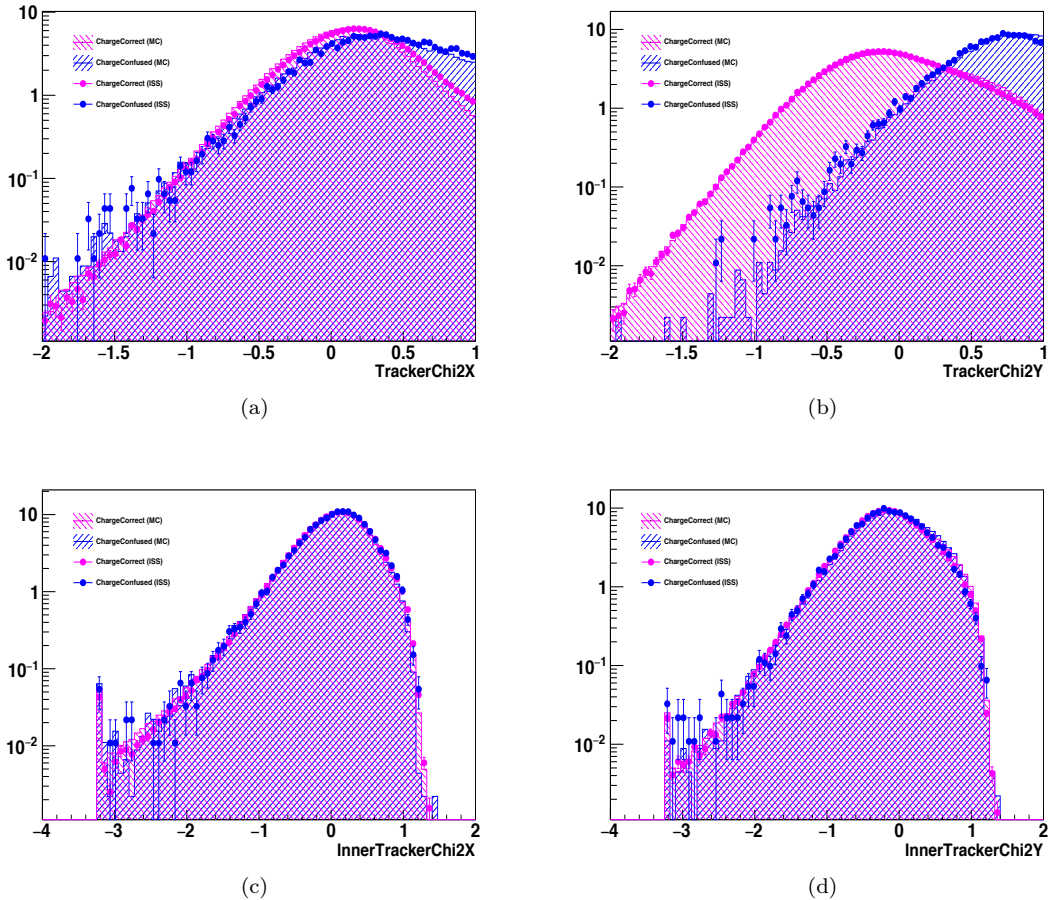


Figure 3: Distributions of a). **TrackerChi2X** b). **TrackerChi2Y** c). **InnerTrackerChi2X** d). **InnerTrackerChi2Y** in example rigidity bin of 330 to 525 GV. Histograms (magenta: charge correct; blue: charge confused) are taken from MC and points (magenta: charge correct; blue: charge confused) are from data.

1265 4. Tracker Charge

1266 Due to the interaction, the tracker charge measurement at the lower part could be con-
1267 taminated. Therefore, this information could be added to the training variable list. The
1268 **TrackerL9Charge** and **TrackerL78Charge** are the two variables related to this. **Track-
1269 erL9Charge** is the tracker charge measurement from layer 9. **TrackerL78Charge** is the
1270 mean value of the tracker charge measurement from layer 7 and 8. In figure 4, the distribu-
1271 tions of the two variables are shown.

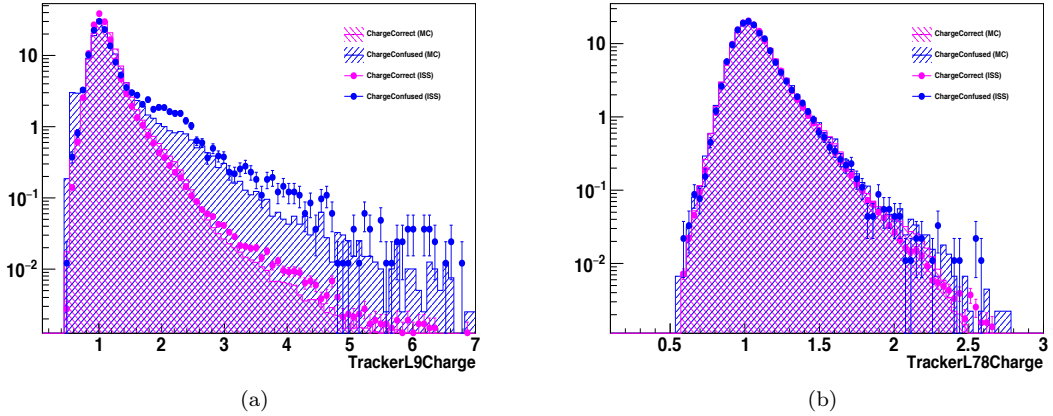


Figure 4: Distributions of a). **TrackerL9Charge** b). **TrackerL78Charge** in example rigidity bin of 330 to 525 GV. Histograms (magenta: charge correct; blue: charge confused) are taken from MC and points (magenta: charge correct; blue: charge confused) are from data.

1272 5. Charge Asymmetry

1273 The tracker charge asymmetry also provides information about charge confusion. **Tracker-**
 1274 **ChargeAsymmetry** is the asymmetry of tracker charge measurements and its definition is
 1275 given below:

$$\text{TrackerChargeAsymmetry} = \frac{\text{TrackerL58Charge} - \text{TrackerL24Charge}}{\text{InnerTrackerCharge}}$$

1276 where the TrackerL58Charge is the mean value of the tracker charge from layer 5 and 8. Track-
 1277 erL24Charge is the mean value of the tracker charge from layer 2 and 4. InnerTrackerCharge
 1278 is the tracker charge from the inner tracker.

1279 In figure 5, the distributions of the **TrackerChargeAsymmetry** is shown.

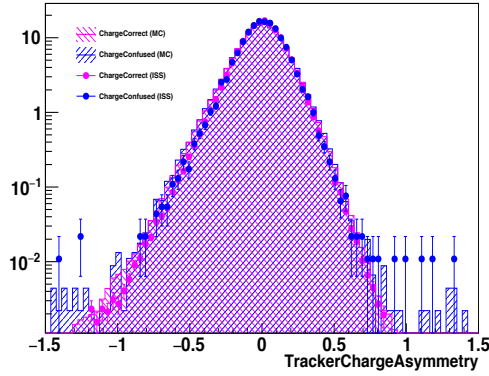


Figure 5: Distributions of **TrackerChargeAsymmetry** in example rigidity bin of 330 to 525 GV. Histograms (magenta: charge correct; blue: charge confused) are taken from MC and points (magenta: charge correct; blue: charge confused) are from data.

1280 6. TRDLikelihood

1281 The last variable is the **TRDLikelihood**. Because of the potential interactions in the TRD
1282 for charge confused events, the **TRDLikelihood** provides the separation power for charge
1283 confusion. In figure 6, the distribution of the **TRDLikelihood** is shown.

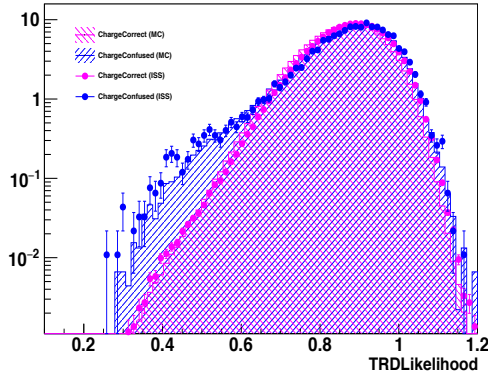


Figure 6: Distributions of **TRDLikelihood** in example rigidity bin of 330 to 525 GV. Histograms (magenta: charge correct; blue: charge confused) are taken from MC and points (magenta: charge correct; blue: charge confused) are from data.

APPENDIX

Acronyms

ACC	Anti-Coincidence Counters
AMS	Alpha Magnetic Spectrometer
BDT	Boosted Decision Tree
CALT	China Academy of Launch Vehicle Technology
CC	Charge Confusion
CR	Cosmic Rays
ECAL	Electromagnetic Calorimeter
GCR	Galactic Cosmic Rays
GTB	Gradient Tree Boosting
HCS	Heliospheric Current Sheet
HMF	Heliospheric Magnetic Field
HT	High Threshold
IGRF	International Geomagnetic Reference Field
ISM	Interstellar Medium
ISS	International Space Station
LEO	Low Earth Orbit
LIS	Local Interstellar Spectra

MDR	Maximum Detectable Rigidity
MHD	Magneto-Hydrodynamic
MIP	Minimum Ionizing Particle
MSFC	Marshall Space Flight Center
NM	Neutron Monitor
POCC	Payload Operations Control Centre
PWN	Pulsar Wind Nebula
RICH	Ring-Imaging Cherenkov detector
SAA	South Atlantic Anomaly
SHT	Super High Threshold
SNRs	Supernova Remnants
SSN	Sunspot Number
SVM	Support Vector Machine
TDRS	Tracking and Data Relay Satellites
TOF	Time Of Flight
TOI	Top-Of-Instrument
TRD	Transition Radiation Detector
TTCS	Tracker Thermal Cooling System
WSGT	White Sands Ground Terminal

1286

APPENDIX

1287

Table of Result

- 1288 In table 1, the result of the time-averaged antiproton to proton flux ratio is given. Rigidity is the
1289 absolute rigidity at the top of the AMS-02 detector. $N_{\bar{p}}$ is the number of antiprotons observed in
1290 each rigidity bin rounded to the nearest integer. $\frac{\Phi_{\bar{p}}}{\Phi_p}$ is the antiproton to proton flux ratio. σ_{stat} is
1291 the total statistical uncertainty and σ_{syst} is the total systematic uncertainty.
- 1292 In table 2 to 24, the result of the time-dependent antiproton to proton flux ratio is shown. In total,
1293 the 23 tables show the antiproton to proton flux ratios in 23 six Bartel Rotations time intervals,
1294 from Bartels Rotation 2426 to 2564. In these tables, Rigidity is the absolute rigidity at the top of
1295 the AMS-02 detector. $N_{\bar{p}}$ is the number of antiprotons observed in each rigidity bin rounded to the
1296 nearest integer. $\frac{\Phi_{\bar{p}}}{\Phi_p}$ is the antiproton to proton flux ratio. σ_{stat} is the total statistical uncertainty
1297 and σ_{syst} is the total systematic uncertainty.

Rigidity (GV)	$N_{\bar{p}}$	$\frac{\Phi_{\bar{p}}}{\Phi_p}$	σ_{stat}	σ_{syst}	Rigidity (GV)	$N_{\bar{p}}$	$\frac{\Phi_{\bar{p}}}{\Phi_p}$	σ_{stat}	σ_{syst}
1.00 — 1.16	72	(1.35 0.13 0.15)×10 ⁻⁵			1.16 — 1.33	145	(1.26 0.12 0.11)×10 ⁻⁵		
1.33 — 1.51	257	(1.39 0.11 0.08)×10 ⁻⁵			1.51 — 1.71	487	(1.60 0.08 0.09)×10 ⁻⁵		
1.71 — 1.92	839	(1.97 0.10 0.10)×10 ⁻⁵			1.92 — 2.15	1493	(2.33 0.07 0.10)×10 ⁻⁵		
2.15 — 2.40	2387	(2.86 0.08 0.11)×10 ⁻⁵			2.40 — 2.67	3617	(3.56 0.08 0.14)×10 ⁻⁵		
2.67 — 2.97	5282	(4.22 0.07 0.16)×10 ⁻⁵			2.97 — 3.29	6921	(4.97 0.08 0.19)×10 ⁻⁵		
3.29 — 3.64	9241	(5.68 0.07 0.22)×10 ⁻⁵			3.64 — 4.02	11400	(6.50 0.08 0.25)×10 ⁻⁵		
4.02 — 4.43	13969	(7.61 0.08 0.25)×10 ⁻⁵			4.43 — 4.88	10120	(8.75 0.08 0.30)×10 ⁻⁵		
4.88 — 5.37	10378	(9.72 0.09 0.30)×10 ⁻⁵			5.37 — 5.90	11109	(1.07 0.01 0.03)×10 ⁻⁴		
5.90 — 6.47	11704	(1.16 0.01 0.03)×10 ⁻⁴			6.47 — 7.09	12271	(1.25 0.01 0.03)×10 ⁻⁴		
7.09 — 7.76	12629	(1.33 0.01 0.04)×10 ⁻⁴			7.76 — 8.48	12669	(1.42 0.01 0.04)×10 ⁻⁴		
8.48 — 9.26	12552	(1.50 0.01 0.05)×10 ⁻⁴			9.26 — 10.1	12325	(1.59 0.01 0.05)×10 ⁻⁴		
10.1 — 11.0	11982	(1.66 0.01 0.04)×10 ⁻⁴			11.0 — 12.0	11890	(1.73 0.02 0.04)×10 ⁻⁴		
12.0 — 13.0	10799	(1.79 0.02 0.05)×10 ⁻⁴			13.0 — 14.1	10832	(1.84 0.02 0.04)×10 ⁻⁴		
14.1 — 15.3	10809	(1.88 0.02 0.04)×10 ⁻⁴			15.3 — 16.6	30786	(1.91 0.01 0.04)×10 ⁻⁴		
16.6 — 18.0	27633	(1.93 0.01 0.05)×10 ⁻⁴			18.0 — 19.5	24262	(1.95 0.01 0.06)×10 ⁻⁴		
19.5 — 21.1	21967	(1.97 0.01 0.06)×10 ⁻⁴			21.1 — 22.8	20127	(1.98 0.01 0.05)×10 ⁻⁴		
22.8 — 24.7	19814	(1.98 0.02 0.04)×10 ⁻⁴			24.7 — 26.7	18383	(1.98 0.01 0.06)×10 ⁻⁴		
26.7 — 28.8	17107	(1.98 0.02 0.05)×10 ⁻⁴			28.8 — 31.1	16345	(1.98 0.02 0.06)×10 ⁻⁴		
31.1 — 33.5	14786	(1.98 0.02 0.06)×10 ⁻⁴			33.5 — 36.1	13835	(1.98 0.02 0.04)×10 ⁻⁴		
36.1 — 38.9	5674	(1.95 0.03 0.06)×10 ⁻⁴			38.9 — 41.9	4830	(1.93 0.03 0.06)×10 ⁻⁴		
41.9 — 45.1	4039	(1.92 0.03 0.05)×10 ⁻⁴			45.1 — 48.5	3429	(1.91 0.03 0.05)×10 ⁻⁴		
48.5 — 52.5	2993	(1.92 0.04 0.05)×10 ⁻⁴			52.2 — 56.1	2547	(1.92 0.04 0.03)×10 ⁻⁴		
56.1 — 60.3	2223	(1.92 0.05 0.06)×10 ⁻⁴			60.3 — 64.8	1918	(1.91 0.05 0.05)×10 ⁻⁴		
64.8 — 69.7	1664	(1.88 0.05 0.05)×10 ⁻⁴			69.7 — 74.9	1424	(1.85 0.06 0.05)×10 ⁻⁴		
74.9 — 80.5	1233	(1.81 0.06 0.04)×10 ⁻⁴			80.5 — 93.0	2005	(1.76 0.05 0.05)×10 ⁻⁴		
93.0 — 108	1596	(1.72 0.06 0.05)×10 ⁻⁴			108 — 125	1214	(1.76 0.07 0.04)×10 ⁻⁴		
125 — 147	1091	(1.93 0.09 0.05)×10 ⁻⁴			147 — 175	402	(2.00 0.14 0.06)×10 ⁻⁴		
175 — 211	143	(1.91 0.19 0.06)×10 ⁻⁴			211 — 259	100	(2.05 0.28 0.09)×10 ⁻⁴		
259 — 330	102	(1.96 0.30 0.17)×10 ⁻⁴			330 — 525	85	(1.82 0.43 0.62)×10 ⁻⁴		

Table 1: Table of time-averaged antiproton to proton flux ratio.

Rigidity (GV)	$N_{\bar{p}}$	$\frac{\Phi_{\bar{p}}}{\Phi_p}$	σ_{stat}	σ_{syst}	Rigidity (GV)	$N_{\bar{p}}$	$\frac{\Phi_{\bar{p}}}{\Phi_p}$	σ_{stat}	σ_{syst}
1.16 — 1.51	42	(1.78	0.25	$0.12) \times 10^{-5}$	5.37 — 6.47	1152	(1.29	0.04	$0.05) \times 10^{-4}$
1.51 — 1.92	87	(1.90	0.23	$0.20) \times 10^{-5}$	6.47 — 7.76	1156	(1.41	0.04	$0.05) \times 10^{-4}$
1.92 — 2.40	226	(2.61	0.21	$0.16) \times 10^{-5}$	7.76 — 9.26	1142	(1.58	0.04	$0.06) \times 10^{-4}$
2.40 — 2.97	509	(4.20	0.23	$0.22) \times 10^{-5}$	9.26 — 11.0	1148	(1.76	0.05	$0.06) \times 10^{-4}$
2.97 — 3.64	825	(5.52	0.23	$0.28) \times 10^{-5}$	11.0 — 13.0	996	(1.81	0.05	$0.06) \times 10^{-4}$
3.64 — 4.43	997	(9.15	0.27	$0.35) \times 10^{-5}$	13.0 — 15.3	864	(1.85	0.06	$0.06) \times 10^{-4}$
4.43 — 5.37	937	(10.1	0.30	$0.35) \times 10^{-5}$	15.3 — 18.0	744	(1.84	0.06	$0.06) \times 10^{-4}$

Table 2: For Bartels Rotation 2426 to 2432 (May 15, 2011 – Oct 24, 2011), the observed antiproton numbers, antiproton to proton flux ratio and the respective statistical and systematic uncertainties.

Rigidity (GV)	$N_{\bar{p}}$	$\frac{\Phi_{\bar{p}}}{\Phi_p}$	σ_{stat}	σ_{syst}	Rigidity (GV)	$N_{\bar{p}}$	$\frac{\Phi_{\bar{p}}}{\Phi_p}$	σ_{stat}	σ_{syst}
1.16 — 1.51	39	(1.61	0.23	$0.12) \times 10^{-5}$	5.37 — 6.47	1167	(1.15	0.03	$0.04) \times 10^{-4}$
1.51 — 1.92	84	(1.75	0.22	$0.16) \times 10^{-5}$	6.47 — 7.76	1287	(1.36	0.03	$0.06) \times 10^{-4}$
1.92 — 2.40	234	(2.61	0.22	$0.17) \times 10^{-5}$	7.76 — 9.26	1264	(1.51	0.04	$0.07) \times 10^{-4}$
2.40 — 2.97	488	(3.89	0.23	$0.23) \times 10^{-5}$	9.26 — 11.0	1275	(1.68	0.04	$0.06) \times 10^{-4}$
2.97 — 3.64	869	(5.58	0.23	$0.30) \times 10^{-5}$	11.0 — 13.0	1140	(1.76	0.05	$0.06) \times 10^{-4}$
3.64 — 4.43	948	(8.04	0.25	$0.32) \times 10^{-5}$	13.0 — 15.3	1042	(1.91	0.05	$0.09) \times 10^{-4}$
4.43 — 5.37	986	(9.59	0.28	$0.35) \times 10^{-5}$	15.3 — 18.0	941	(1.98	0.06	$0.07) \times 10^{-4}$

Table 3: For Bartels Rotation 2432 to 2438 (Oct 24, 2011 – Apr 03, 2012), the observed antiproton numbers, antiproton to proton flux ratio and the respective statistical and systematic uncertainties.

Rigidity (GV)	$N_{\bar{p}}$	$\frac{\Phi_{\bar{p}}}{\Phi_p}$	σ_{stat}	σ_{syst}	Rigidity (GV)	$N_{\bar{p}}$	$\frac{\Phi_{\bar{p}}}{\Phi_p}$	σ_{stat}	σ_{syst}
1.16 — 1.51	41	(2.43	0.33	$0.15) \times 10^{-5}$	5.37 — 6.47	1184	(1.23	0.03	$0.04) \times 10^{-4}$
1.51 — 1.92	92	(2.75	0.31	$0.20) \times 10^{-5}$	6.47 — 7.76	1277	(1.42	0.04	$0.05) \times 10^{-4}$
1.92 — 2.40	242	(3.48	0.27	$0.21) \times 10^{-5}$	7.76 — 9.26	1265	(1.59	0.04	$0.07) \times 10^{-4}$
2.40 — 2.97	491	(4.67	0.26	$0.27) \times 10^{-5}$	9.26 — 11.0	1170	(1.62	0.04	$0.08) \times 10^{-4}$
2.97 — 3.64	841	(6.12	0.25	$0.33) \times 10^{-5}$	11.0 — 13.0	1131	(1.83	0.05	$0.07) \times 10^{-4}$
3.64 — 4.43	928	(8.22	0.25	$0.39) \times 10^{-5}$	13.0 — 15.3	935	(1.78	0.05	$0.05) \times 10^{-4}$
4.43 — 5.37	1011	(10.2	0.29	$0.37) \times 10^{-5}$	15.3 — 18.0	940	(2.01	0.06	$0.07) \times 10^{-4}$

Table 4: For Bartels Rotation 2438 to 2444 (Apr 03, 2012 – Sep 12, 2012), the observed antiproton numbers, antiproton to proton flux ratio and the respective statistical and systematic uncertainties.

Rigidity (GV)	$N_{\bar{p}}$	$\frac{\Phi_{\bar{p}}}{\Phi_p}$	σ_{stat}	σ_{syst}	Rigidity (GV)	$N_{\bar{p}}$	$\frac{\Phi_{\bar{p}}}{\Phi_p}$	σ_{stat}	σ_{syst}
1.16 — 1.51	57	(2.24	0.28	$0.16) \times 10^{-5}$	5.37 — 6.47	1302	(1.19	0.03	$0.04) \times 10^{-4}$
1.51 — 1.92	143	(2.77	0.24	$0.15) \times 10^{-5}$	6.47 — 7.76	1355	(1.35	0.03	$0.04) \times 10^{-4}$
1.92 — 2.40	331	(3.42	0.23	$0.23) \times 10^{-5}$	7.76 — 9.26	1409	(1.60	0.04	$0.06) \times 10^{-4}$
2.40 — 2.97	592	(4.34	0.22	$0.25) \times 10^{-5}$	9.26 — 11.0	1322	(1.67	0.04	$0.06) \times 10^{-4}$
2.97 — 3.64	955	(5.63	0.21	$0.27) \times 10^{-5}$	11.0 — 13.0	1213	(1.81	0.05	$0.09) \times 10^{-4}$
3.64 — 4.43	1121	(8.65	0.24	$0.33) \times 10^{-5}$	13.0 — 15.3	1114	(1.97	0.05	$0.09) \times 10^{-4}$
4.43 — 5.37	1149	(10.2	0.27	$0.36) \times 10^{-5}$	15.3 — 18.0	951	(1.95	0.06	$0.07) \times 10^{-4}$

Table 5: For Bartels Rotation 2444 to 2450 (Sep 12, 2012 – Feb 21, 2013), the observed antiproton numbers, antiproton to proton flux ratio and the respective statistical and systematic uncertainties.

Rigidity (GV)	$N_{\bar{p}}$	$\frac{\Phi_{\bar{p}}}{\Phi_p}$	σ_{stat}	σ_{syst}	Rigidity (GV)	$N_{\bar{p}}$	$\frac{\Phi_{\bar{p}}}{\Phi_p}$	σ_{stat}	σ_{syst}
1.16 — 1.51	27	(1.64	0.32	$0.12) \times 10^{-5}$	5.37 — 6.47	1200	(1.16	0.03	$0.04) \times 10^{-4}$
1.51 — 1.92	86	(2.64	0.31	$0.20) \times 10^{-5}$	6.47 — 7.76	1308	(1.36	0.03	$0.05) \times 10^{-4}$
1.92 — 2.40	203	(2.88	0.25	$0.22) \times 10^{-5}$	7.76 — 9.26	1269	(1.49	0.04	$0.05) \times 10^{-4}$
2.40 — 2.97	561	(5.15	0.26	$0.27) \times 10^{-5}$	9.26 — 11.0	1247	(1.62	0.04	$0.06) \times 10^{-4}$
2.97 — 3.64	857	(5.96	0.25	$0.29) \times 10^{-5}$	11.0 — 13.0	1184	(1.81	0.05	$0.09) \times 10^{-4}$
3.64 — 4.43	972	(8.17	0.24	$0.32) \times 10^{-5}$	13.0 — 15.3	1010	(1.82	0.05	$0.08) \times 10^{-4}$
4.43 — 5.37	1063	(10.1	0.28	$0.40) \times 10^{-5}$	15.3 — 18.0	960	(2.00	0.06	$0.06) \times 10^{-4}$

Table 6: For Bartels Rotation 2450 to 2456 (Feb 21, 2013 – Aug 02, 2013), the observed antiproton numbers, antiproton to proton flux ratio and the respective statistical and systematic uncertainties.

Rigidity (GV)	$N_{\bar{p}}$	$\frac{\Phi_{\bar{p}}}{\Phi_p}$	σ_{stat}	σ_{syst}	Rigidity (GV)	$N_{\bar{p}}$	$\frac{\Phi_{\bar{p}}}{\Phi_p}$	σ_{stat}	σ_{syst}
1.16 — 1.51	52	(2.52	0.33	$0.15) \times 10^{-5}$	5.37 — 6.47	1283	(1.15	0.03	$0.03) \times 10^{-4}$
1.51 — 1.92	130	(2.84	0.27	$0.21) \times 10^{-5}$	6.47 — 7.76	1419	(1.38	0.03	$0.05) \times 10^{-4}$
1.92 — 2.40	293	(3.15	0.22	$0.14) \times 10^{-5}$	7.76 — 9.26	1336	(1.48	0.04	$0.05) \times 10^{-4}$
2.40 — 2.97	527	(3.88	0.21	$0.19) \times 10^{-5}$	9.26 — 11.0	1297	(1.61	0.04	$0.05) \times 10^{-4}$
2.97 — 3.64	1002	(5.79	0.22	$0.27) \times 10^{-5}$	11.0 — 13.0	1248	(1.84	0.05	$0.08) \times 10^{-4}$
3.64 — 4.43	1141	(8.66	0.23	$0.33) \times 10^{-5}$	13.0 — 15.3	1063	(1.86	0.05	$0.06) \times 10^{-4}$
4.43 — 5.37	1130	(9.88	0.27	$0.34) \times 10^{-5}$	15.3 — 18.0	977	(1.99	0.06	$0.06) \times 10^{-4}$

Table 7: For Bartels Rotation 2456 to 2462 (Aug 02, 2013 – Jan 11, 2014), the observed antiproton numbers, antiproton to proton flux ratio and the respective statistical and systematic uncertainties.

Rigidity (GV)	$N_{\bar{p}}$	$\frac{\Phi_{\bar{p}}}{\Phi_p}$	σ_{stat}	σ_{syst}	Rigidity (GV)	$N_{\bar{p}}$	$\frac{\Phi_{\bar{p}}}{\Phi_p}$	σ_{stat}	σ_{syst}
1.16 — 1.51	51	(2.06	0.28	$0.14) \times 10^{-5}$	5.37 — 6.47	1442	(1.19	0.03	$0.03) \times 10^{-4}$
1.51 — 1.92	152	(2.76	0.24	$0.18) \times 10^{-5}$	6.47 — 7.76	1500	(1.35	0.03	$0.04) \times 10^{-4}$
1.92 — 2.40	358	(3.30	0.21	$0.16) \times 10^{-5}$	7.76 — 9.26	1458	(1.50	0.04	$0.05) \times 10^{-4}$
2.40 — 2.97	711	(4.57	0.21	$0.22) \times 10^{-5}$	9.26 — 11.0	1469	(1.69	0.04	$0.07) \times 10^{-4}$
2.97 — 3.64	1038	(5.31	0.20	$0.25) \times 10^{-5}$	11.0 — 13.0	1306	(1.78	0.04	$0.07) \times 10^{-4}$
3.64 — 4.43	1207	(8.29	0.22	$0.32) \times 10^{-5}$	13.0 — 15.3	1161	(1.88	0.05	$0.05) \times 10^{-4}$
4.43 — 5.37	1254	(10.0	0.26	$0.39) \times 10^{-5}$	15.3 — 18.0	1042	(1.96	0.06	$0.06) \times 10^{-4}$

Table 8: For Bartels Rotation 2462 to 2468 (Jan 11, 2014 – Jun 22, 2014), the observed antiproton numbers, antiproton to proton flux ratio and the respective statistical and systematic uncertainties.

Rigidity (GV)	$N_{\bar{p}}$	$\frac{\Phi_{\bar{p}}}{\Phi_p}$	σ_{stat}	σ_{syst}	Rigidity (GV)	$N_{\bar{p}}$	$\frac{\Phi_{\bar{p}}}{\Phi_p}$	σ_{stat}	σ_{syst}
1.16 — 1.51	27	(1.71	0.30	$0.11) \times 10^{-5}$	5.37 — 6.47	886	(1.18	0.04	$0.03) \times 10^{-4}$
1.51 — 1.92	85	(2.38	0.26	$0.16) \times 10^{-5}$	6.47 — 7.76	885	(1.29	0.04	$0.04) \times 10^{-4}$
1.92 — 2.40	258	(3.71	0.27	$0.21) \times 10^{-5}$	7.76 — 9.26	828	(1.38	0.04	$0.06) \times 10^{-4}$
2.40 — 2.97	367	(3.70	0.23	$0.20) \times 10^{-5}$	9.26 — 11.0	881	(1.65	0.05	$0.07) \times 10^{-4}$
2.97 — 3.64	605	(4.90	0.23	$0.24) \times 10^{-5}$	11.0 — 13.0	803	(1.78	0.06	$0.09) \times 10^{-4}$
3.64 — 4.43	779	(8.62	0.28	$0.31) \times 10^{-5}$	13.0 — 15.3	747	(1.98	0.06	$0.07) \times 10^{-4}$
4.43 — 5.37	746	(9.63	0.32	$0.36) \times 10^{-5}$	15.3 — 18.0	614	(1.90	0.07	$0.08) \times 10^{-4}$

Table 9: For Bartels Rotation 2468 to 2474 (Jun 22, 2014 – Dec 01, 2014), the observed antiproton numbers, antiproton to proton flux ratio and the respective statistical and systematic uncertainties.

Rigidity (GV)	$N_{\bar{p}}$	$\frac{\Phi_{\bar{p}}}{\Phi_p}$	σ_{stat}	σ_{syst}	Rigidity (GV)	$N_{\bar{p}}$	$\frac{\Phi_{\bar{p}}}{\Phi_p}$	σ_{stat}	σ_{syst}
1.16 — 1.51	43	(2.15	0.31	$0.19) \times 10^{-5}$	5.37 — 6.47	1247	(1.15	0.03	$0.03) \times 10^{-4}$
1.51 — 1.92	110	(2.76	0.29	$0.23) \times 10^{-5}$	6.47 — 7.76	1322	(1.32	0.03	$0.04) \times 10^{-4}$
1.92 — 2.40	244	(3.02	0.23	$0.17) \times 10^{-5}$	7.76 — 9.26	1300	(1.47	0.04	$0.05) \times 10^{-4}$
2.40 — 2.97	458	(3.78	0.22	$0.17) \times 10^{-5}$	9.26 — 11.0	1358	(1.70	0.04	$0.08) \times 10^{-4}$
2.97 — 3.64	870	(5.57	0.22	$0.26) \times 10^{-5}$	11.0 — 13.0	1257	(1.85	0.05	$0.06) \times 10^{-4}$
3.64 — 4.43	984	(7.72	0.23	$0.30) \times 10^{-5}$	13.0 — 15.3	1134	(1.97	0.05	$0.05) \times 10^{-4}$
4.43 — 5.37	1065	(9.58	0.27	$0.33) \times 10^{-5}$	15.3 — 18.0	925	(1.85	0.06	$0.08) \times 10^{-4}$

Table 10: For Bartels Rotation 2474 to 2480 (Dec 01, 2014 – May 12, 2015), the observed antiproton numbers, antiproton to proton flux ratio and the respective statistical and systematic uncertainties.

Rigidity (GV)	$N_{\bar{p}}$	$\frac{\Phi_{\bar{p}}}{\Phi_p}$	σ_{stat}	σ_{syst}	Rigidity (GV)	$N_{\bar{p}}$	$\frac{\Phi_{\bar{p}}}{\Phi_p}$	σ_{stat}	σ_{syst}
1.16 — 1.51	47	(3.12	0.40	$0.23) \times 10^{-5}$	5.37 — 6.47	1133	(1.11	0.03	$0.04) \times 10^{-4}$
1.51 — 1.92	85	(2.91	0.34	$0.17) \times 10^{-5}$	6.47 — 7.76	1242	(1.31	0.03	$0.04) \times 10^{-4}$
1.92 — 2.40	213	(3.31	0.27	$0.23) \times 10^{-5}$	7.76 — 9.26	1236	(1.48	0.04	$0.06) \times 10^{-4}$
2.40 — 2.97	392	(3.87	0.25	$0.24) \times 10^{-5}$	9.26 — 11.0	1262	(1.66	0.04	$0.06) \times 10^{-4}$
2.97 — 3.64	708	(5.24	0.23	$0.24) \times 10^{-5}$	11.0 — 13.0	1141	(1.76	0.05	$0.07) \times 10^{-4}$
3.64 — 4.43	878	(7.44	0.23	$0.31) \times 10^{-5}$	13.0 — 15.3	1083	(1.97	0.05	$0.08) \times 10^{-4}$
4.43 — 5.37	947	(9.05	0.27	$0.32) \times 10^{-5}$	15.3 — 18.0	947	(1.97	0.06	$0.07) \times 10^{-4}$

Table 11: For Bartels Rotation 2480 to 2486 (May 12, 2015 – Oct 21, 2015), the observed antiproton numbers, antiproton to proton flux ratio and the respective statistical and systematic uncertainties.

Rigidity (GV)	$N_{\bar{p}}$	$\frac{\Phi_{\bar{p}}}{\Phi_p}$	σ_{stat}	σ_{syst}	Rigidity (GV)	$N_{\bar{p}}$	$\frac{\Phi_{\bar{p}}}{\Phi_p}$	σ_{stat}	σ_{syst}
1.16 — 1.51	23	(1.36	0.26	$0.14) \times 10^{-5}$	5.37 — 6.47	1188	(1.13	0.03	$0.04) \times 10^{-4}$
1.51 — 1.92	59	(1.81	0.26	$0.12) \times 10^{-5}$	6.47 — 7.76	1191	(1.23	0.03	$0.04) \times 10^{-4}$
1.92 — 2.40	189	(2.65	0.23	$0.14) \times 10^{-5}$	7.76 — 9.26	1195	(1.41	0.04	$0.05) \times 10^{-4}$
2.40 — 2.97	404	(3.63	0.22	$0.21) \times 10^{-5}$	9.26 — 11.0	1274	(1.66	0.04	$0.06) \times 10^{-4}$
2.97 — 3.64	726	(4.94	0.22	$0.25) \times 10^{-5}$	11.0 — 13.0	1180	(1.81	0.05	$0.09) \times 10^{-4}$
3.64 — 4.43	931	(7.62	0.23	$0.28) \times 10^{-5}$	13.0 — 15.3	1047	(1.90	0.05	$0.07) \times 10^{-4}$
4.43 — 5.37	981	(9.06	0.26	$0.33) \times 10^{-5}$	15.3 — 18.0	917	(1.91	0.06	$0.10) \times 10^{-4}$

Table 12: For Bartels Rotation 2486 to 2492 (Oct 21, 2015 – Mar 31, 2016), the observed antiproton numbers, antiproton to proton flux ratio and the respective statistical and systematic uncertainties.

Rigidity (GV)	$N_{\bar{p}}$	$\frac{\Phi_{\bar{p}}}{\Phi_p}$	σ_{stat}	σ_{syst}	Rigidity (GV)	$N_{\bar{p}}$	$\frac{\Phi_{\bar{p}}}{\Phi_p}$	σ_{stat}	σ_{syst}
1.16 — 1.51	29	(1.74	0.29	$0.17) \times 10^{-5}$	5.37 — 6.47	1127	(1.05	0.03	$0.04) \times 10^{-4}$
1.51 — 1.92	84	(2.43	0.29	$0.15) \times 10^{-5}$	6.47 — 7.76	1178	(1.20	0.03	$0.04) \times 10^{-4}$
1.92 — 2.40	173	(2.22	0.20	$0.15) \times 10^{-5}$	7.76 — 9.26	1185	(1.39	0.04	$0.05) \times 10^{-4}$
2.40 — 2.97	394	(3.29	0.21	$0.22) \times 10^{-5}$	9.26 — 11.0	1230	(1.60	0.04	$0.05) \times 10^{-4}$
2.97 — 3.64	721	(4.62	0.20	$0.22) \times 10^{-5}$	11.0 — 13.0	1148	(1.76	0.05	$0.09) \times 10^{-4}$
3.64 — 4.43	883	(7.03	0.22	$0.25) \times 10^{-5}$	13.0 — 15.3	996	(1.81	0.05	$0.05) \times 10^{-4}$
4.43 — 5.37	989	(8.94	0.26	$0.32) \times 10^{-5}$	15.3 — 18.0	939	(1.96	0.06	$0.06) \times 10^{-4}$

Table 13: For Bartels Rotation 2492 to 2498 (Mar 31, 2016 – Sep 09, 2016), the observed antiproton numbers, antiproton to proton flux ratio and the respective statistical and systematic uncertainties.

Rigidity (GV)	$N_{\bar{p}}$	$\frac{\Phi_{\bar{p}}}{\Phi_p}$	σ_{stat}	σ_{syst}	Rigidity (GV)	$N_{\bar{p}}$	$\frac{\Phi_{\bar{p}}}{\Phi_p}$	σ_{stat}	σ_{syst}
1.16 — 1.51	31	(2.22	0.37	$0.18) \times 10^{-5}$	5.37 — 6.47	1153	(1.09	0.03	$0.04) \times 10^{-4}$
1.51 — 1.92	41	(1.36	0.23	$0.10) \times 10^{-5}$	6.47 — 7.76	1189	(1.23	0.03	$0.04) \times 10^{-4}$
1.92 — 2.40	182	(2.54	0.23	$0.16) \times 10^{-5}$	7.76 — 9.26	1295	(1.53	0.04	$0.06) \times 10^{-4}$
2.40 — 2.97	344	(3.05	0.21	$0.19) \times 10^{-5}$	9.26 — 11.0	1249	(1.63	0.04	$0.05) \times 10^{-4}$
2.97 — 3.64	622	(4.17	0.20	$0.21) \times 10^{-5}$	11.0 — 13.0	1179	(1.82	0.05	$0.07) \times 10^{-4}$
3.64 — 4.43	849	(7.05	0.22	$0.26) \times 10^{-5}$	13.0 — 15.3	997	(1.82	0.05	$0.06) \times 10^{-4}$
4.43 — 5.37	926	(8.63	0.26	$0.32) \times 10^{-5}$	15.3 — 18.0	946	(1.98	0.06	$0.10) \times 10^{-4}$

Table 14: For Bartels Rotation 2498 to 2504 (Sep 09, 2016 – Feb 18, 2017), the observed antiproton numbers, antiproton to proton flux ratio and the respective statistical and systematic uncertainties.

Rigidity (GV)	$N_{\bar{p}}$	$\frac{\Phi_{\bar{p}}}{\Phi_p}$	σ_{stat}	σ_{syst}	Rigidity (GV)	$N_{\bar{p}}$	$\frac{\Phi_{\bar{p}}}{\Phi_p}$	σ_{stat}	σ_{syst}
1.16 — 1.51	36	(2.48	0.38	$0.17) \times 10^{-5}$	5.37 — 6.47	1137	(1.14	0.03	$0.04) \times 10^{-4}$
1.51 — 1.92	46	(1.62	0.28	$0.22) \times 10^{-5}$	6.47 — 7.76	1170	(1.28	0.03	$0.04) \times 10^{-4}$
1.92 — 2.40	150	(2.34	0.23	$0.15) \times 10^{-5}$	7.76 — 9.26	1155	(1.44	0.04	$0.07) \times 10^{-4}$
2.40 — 2.97	347	(3.42	0.22	$0.21) \times 10^{-5}$	9.26 — 11.0	1154	(1.60	0.04	$0.11) \times 10^{-4}$
2.97 — 3.64	558	(4.13	0.21	$0.22) \times 10^{-5}$	11.0 — 13.0	1038	(1.69	0.05	$0.09) \times 10^{-4}$
3.64 — 4.43	809	(7.34	0.23	$0.32) \times 10^{-5}$	13.0 — 15.3	1008	(1.94	0.06	$0.06) \times 10^{-4}$
4.43 — 5.37	920	(9.27	0.28	$0.31) \times 10^{-5}$	15.3 — 18.0	869	(1.91	0.06	$0.06) \times 10^{-4}$

Table 15: For Bartels Rotation 2504 to 2510 (Feb 18, 2017 – Jul 30, 2017), the observed antiproton numbers, antiproton to proton flux ratio and the respective statistical and systematic uncertainties.

Rigidity (GV)	$N_{\bar{p}}$	$\frac{\Phi_{\bar{p}}}{\Phi_p}$	σ_{stat}	σ_{syst}	Rigidity (GV)	$N_{\bar{p}}$	$\frac{\Phi_{\bar{p}}}{\Phi_p}$	σ_{stat}	σ_{syst}
1.16 — 1.51	40	(2.39	0.36	$0.19) \times 10^{-5}$	5.37 — 6.47	1101	(1.06	0.03	$0.03) \times 10^{-4}$
1.51 — 1.92	60	(1.91	0.28	$0.15) \times 10^{-5}$	6.47 — 7.76	1224	(1.28	0.03	$0.04) \times 10^{-4}$
1.92 — 2.40	152	(2.27	0.22	$0.14) \times 10^{-5}$	7.76 — 9.26	1251	(1.48	0.04	$0.06) \times 10^{-4}$
2.40 — 2.97	319	(3.07	0.22	$0.16) \times 10^{-5}$	9.26 — 11.0	1292	(1.69	0.04	$0.06) \times 10^{-4}$
2.97 — 3.64	632	(4.64	0.22	$0.29) \times 10^{-5}$	11.0 — 13.0	1095	(1.67	0.05	$0.11) \times 10^{-4}$
3.64 — 4.43	759	(6.78	0.23	$0.27) \times 10^{-5}$	13.0 — 15.3	1030	(1.84	0.05	$0.05) \times 10^{-4}$
4.43 — 5.37	967	(9.43	0.28	$0.34) \times 10^{-5}$	15.3 — 18.0	928	(1.91	0.06	$0.11) \times 10^{-4}$

Table 16: For Bartels Rotation 2510 to 2516 (Jul 30, 2017 – Jan 08, 2018), the observed antiproton numbers, antiproton to proton flux ratio and the respective statistical and systematic uncertainties.

Rigidity (GV)	$N_{\bar{p}}$	$\frac{\Phi_{\bar{p}}}{\Phi_p}$	σ_{stat}	σ_{syst}	Rigidity (GV)	$N_{\bar{p}}$	$\frac{\Phi_{\bar{p}}}{\Phi_p}$	σ_{stat}	σ_{syst}
1.16 — 1.51	29	(1.36 0.24 0.15)×10 ⁻⁵			5.37 — 6.47	1263	(1.16 0.03 0.04)×10 ⁻⁴		
1.51 — 1.92	75	(1.80 0.24 0.14)×10 ⁻⁵			6.47 — 7.76	1245	(1.25 0.03 0.04)×10 ⁻⁴		
1.92 — 2.40	190	(2.21 0.19 0.15)×10 ⁻⁵			7.76 — 9.26	1289	(1.49 0.04 0.07)×10 ⁻⁴		
2.40 — 2.97	374	(2.98 0.19 0.15)×10 ⁻⁵			9.26 — 11.0	1269	(1.63 0.04 0.06)×10 ⁻⁴		
2.97 — 3.64	709	(4.44 0.20 0.20)×10 ⁻⁵			11.0 — 13.0	1203	(1.82 0.05 0.05)×10 ⁻⁴		
3.64 — 4.43	870	(7.15 0.22 0.30)×10 ⁻⁵			13.0 — 15.3	1015	(1.82 0.05 0.05)×10 ⁻⁴		
4.43 — 5.37	986	(9.08 0.27 0.34)×10 ⁻⁵			15.3 — 18.0	938	(1.93 0.06 0.12)×10 ⁻⁴		

Table 17: For Bartels Rotation 2516 to 2522 (Jan 08, 2018 – Jun 19, 2018), the observed antiproton numbers, antiproton to proton flux ratio and the respective statistical and systematic uncertainties.

Rigidity (GV)	$N_{\bar{p}}$	$\frac{\Phi_{\bar{p}}}{\Phi_p}$	σ_{stat}	σ_{syst}	Rigidity (GV)	$N_{\bar{p}}$	$\frac{\Phi_{\bar{p}}}{\Phi_p}$	σ_{stat}	σ_{syst}
1.16 — 1.51	20	(1.85 0.37 0.23)×10 ⁻⁵			5.37 — 6.47	758	(1.17 0.04 0.05)×10 ⁻⁴		
1.51 — 1.92	40	(1.89 0.32 0.30)×10 ⁻⁵			6.47 — 7.76	777	(1.31 0.04 0.05)×10 ⁻⁴		
1.92 — 2.40	104	(2.29 0.26 0.16)×10 ⁻⁵			7.76 — 9.26	768	(1.48 0.05 0.07)×10 ⁻⁴		
2.40 — 2.97	230	(3.33 0.26 0.20)×10 ⁻⁵			9.26 — 11.0	816	(1.74 0.05 0.09)×10 ⁻⁴		
2.97 — 3.64	401	(4.49 0.26 0.26)×10 ⁻⁵			11.0 — 13.0	713	(1.79 0.06 0.07)×10 ⁻⁴		
3.64 — 4.43	517	(7.28 0.29 0.26)×10 ⁻⁵			13.0 — 15.3	669	(1.98 0.07 0.07)×10 ⁻⁴		
4.43 — 5.37	601	(9.35 0.35 0.33)×10 ⁻⁵			15.3 — 18.0	574	(1.95 0.07 0.12)×10 ⁻⁴		

Table 18: For Bartels Rotation 2522 to 2528 (Jun 19, 2018 – Nov 28, 2018), the observed antiproton numbers, antiproton to proton flux ratio and the respective statistical and systematic uncertainties.

Rigidity (GV)	$N_{\bar{p}}$	$\frac{\Phi_{\bar{p}}}{\Phi_p}$	σ_{stat}	σ_{syst}	Rigidity (GV)	$N_{\bar{p}}$	$\frac{\Phi_{\bar{p}}}{\Phi_p}$	σ_{stat}	σ_{syst}
1.16 — 1.51	31	(2.25 0.37 0.20)×10 ⁻⁵			5.37 — 6.47	680	(1.05 0.04 0.04)×10 ⁻⁴		
1.51 — 1.92	45	(1.59 0.26 0.17)×10 ⁻⁵			6.47 — 7.76	767	(1.30 0.04 0.04)×10 ⁻⁴		
1.92 — 2.40	97	(1.76 0.21 0.15)×10 ⁻⁵			7.76 — 9.26	819	(1.60 0.05 0.06)×10 ⁻⁴		
2.40 — 2.97	224	(2.87 0.23 0.17)×10 ⁻⁵			9.26 — 11.0	719	(1.57 0.05 0.05)×10 ⁻⁴		
2.97 — 3.64	380	(3.88 0.22 0.21)×10 ⁻⁵			11.0 — 13.0	736	(1.90 0.06 0.05)×10 ⁻⁴		
3.64 — 4.43	564	(7.76 0.30 0.32)×10 ⁻⁵			13.0 — 15.3	593	(1.82 0.07 0.07)×10 ⁻⁴		
4.43 — 5.37	572	(8.84 0.33 0.30)×10 ⁻⁵			15.3 — 18.0	556	(1.96 0.08 0.07)×10 ⁻⁴		

Table 19: For Bartels Rotation 2528 to 2534 (Nov 28, 2018 – May 09, 2019), the observed antiproton numbers, antiproton to proton flux ratio and the respective statistical and systematic uncertainties.

Rigidity (GV)	$N_{\bar{p}}$	$\frac{\Phi_{\bar{p}}}{\Phi_p}$	σ_{stat}	σ_{syst}	Rigidity (GV)	$N_{\bar{p}}$	$\frac{\Phi_{\bar{p}}}{\Phi_p}$	σ_{stat}	σ_{syst}
1.16 — 1.51	19	(1.77 0.35 0.14)×10 ⁻⁵			5.37 — 6.47	715	(1.16 0.04 0.04)×10 ⁻⁴		
1.51 — 1.92	42	(2.00 0.33 0.17)×10 ⁻⁵			6.47 — 7.76	741	(1.32 0.04 0.04)×10 ⁻⁴		
1.92 — 2.40	85	(1.90 0.24 0.19)×10 ⁻⁵			7.76 — 9.26	711	(1.45 0.05 0.05)×10 ⁻⁴		
2.40 — 2.97	207	(3.07 0.25 0.25)×10 ⁻⁵			9.26 — 11.0	757	(1.72 0.06 0.08)×10 ⁻⁴		
2.97 — 3.64	359	(4.11 0.25 0.21)×10 ⁻⁵			11.0 — 13.0	725	(1.95 0.06 0.08)×10 ⁻⁴		
3.64 — 4.43	514	(7.59 0.31 0.33)×10 ⁻⁵			13.0 — 15.3	585	(1.86 0.07 0.06)×10 ⁻⁴		
4.43 — 5.37	508	(8.31 0.34 0.35)×10 ⁻⁵			15.3 — 18.0	529	(1.93 0.08 0.11)×10 ⁻⁴		

Table 20: For Bartels Rotation 2534 to 2540 (May 09, 2019 – Oct 18, 2019), the observed antiproton numbers, antiproton to proton flux ratio and the respective statistical and systematic uncertainties.

Rigidity (GV)	$N_{\bar{p}}$	$\frac{\Phi_{\bar{p}}}{\Phi_p}$	σ_{stat}	σ_{syst}	Rigidity (GV)	$N_{\bar{p}}$	$\frac{\Phi_{\bar{p}}}{\Phi_p}$	σ_{stat}	σ_{syst}
1.16 — 1.51	15	(1.74 0.39 0.16)×10 ⁻⁵			5.37 — 6.47	503	(1.10 0.04 0.03)×10 ⁻⁴		
1.51 — 1.92	34	(2.01 0.35 0.16)×10 ⁻⁵			6.47 — 7.76	545	(1.30 0.05 0.04)×10 ⁻⁴		
1.92 — 2.40	83	(2.36 0.30 0.18)×10 ⁻⁵			7.76 — 9.26	541	(1.48 0.06 0.05)×10 ⁻⁴		
2.40 — 2.97	152	(2.96 0.27 0.15)×10 ⁻⁵			9.26 — 11.0	503	(1.54 0.06 0.06)×10 ⁻⁴		
2.97 — 3.64	304	(4.58 0.28 0.23)×10 ⁻⁵			11.0 — 13.0	483	(1.75 0.07 0.07)×10 ⁻⁴		
3.64 — 4.43	331	(6.70 0.34 0.27)×10 ⁻⁵			13.0 — 15.3	435	(1.87 0.08 0.07)×10 ⁻⁴		
4.43 — 5.37	375	(8.36 0.40 0.27)×10 ⁻⁵			15.3 — 18.0	385	(1.91 0.09 0.06)×10 ⁻⁴		

Table 21: For Bartels Rotation 2540 to 2546 (Oct 18, 2019 – Mar 28, 2020), the observed antiproton numbers, antiproton to proton flux ratio and the respective statistical and systematic uncertainties.

Rigidity (GV)	$N_{\bar{p}}$	$\frac{\Phi_{\bar{p}}}{\Phi_p}$	σ_{stat}	σ_{syst}	Rigidity (GV)	$N_{\bar{p}}$	$\frac{\Phi_{\bar{p}}}{\Phi_p}$	σ_{stat}	σ_{syst}
1.16 — 1.51	21	(2.31 0.42 0.28)×10 ⁻⁵			5.37 — 6.47	553	(1.18 0.04 0.04)×10 ⁻⁴		
1.51 — 1.92	49	(2.76 0.40 0.25)×10 ⁻⁵			6.47 — 7.76	549	(1.28 0.05 0.04)×10 ⁻⁴		
1.92 — 2.40	89	(2.48 0.29 0.14)×10 ⁻⁵			7.76 — 9.26	565	(1.52 0.06 0.07)×10 ⁻⁴		
2.40 — 2.97	187	(3.56 0.28 0.23)×10 ⁻⁵			9.26 — 11.0	553	(1.66 0.06 0.08)×10 ⁻⁴		
2.97 — 3.64	321	(4.78 0.29 0.27)×10 ⁻⁵			11.0 — 13.0	521	(1.85 0.07 0.05)×10 ⁻⁴		
3.64 — 4.43	374	(7.48 0.35 0.36)×10 ⁻⁵			13.0 — 15.3	436	(1.84 0.08 0.05)×10 ⁻⁴		
4.43 — 5.37	415	(9.12 0.40 0.32)×10 ⁻⁵			15.3 — 18.0	423	(2.06 0.09 0.06)×10 ⁻⁴		

Table 22: For Bartels Rotation 2546 to 2552 (May 28, 2020 – Sep 06, 2020), the observed antiproton numbers, antiproton to proton flux ratio and the respective statistical and systematic uncertainties.

Rigidity (GV)	$N_{\bar{p}}$	$\frac{\Phi_{\bar{p}}}{\Phi_p}$	σ_{stat}	σ_{syst}	Rigidity (GV)	$N_{\bar{p}}$	$\frac{\Phi_{\bar{p}}}{\Phi_p}$	σ_{stat}	σ_{syst}
1.16 — 1.51	42	(3.07	0.40	$0.35) \times 10^{-5}$	5.37 — 6.47	911	(1.12	0.03	$0.04) \times 10^{-4}$
1.51 — 1.92	52	(1.82	0.29	$0.18) \times 10^{-5}$	6.47 — 7.76	1036	(1.39	0.04	$0.04) \times 10^{-4}$
1.92 — 2.40	136	(2.23	0.22	$0.17) \times 10^{-5}$	7.76 — 9.26	987	(1.52	0.05	$0.06) \times 10^{-4}$
2.40 — 2.97	265	(2.90	0.22	$0.16) \times 10^{-5}$	9.26 — 11.0	993	(1.71	0.05	$0.05) \times 10^{-4}$
2.97 — 3.64	504	(4.27	0.22	$0.23) \times 10^{-5}$	11.0 — 13.0	904	(1.84	0.06	$0.08) \times 10^{-4}$
3.64 — 4.43	689	(7.79	0.27	$0.35) \times 10^{-5}$	13.0 — 15.3	786	(1.89	0.06	$0.10) \times 10^{-4}$
4.43 — 5.37	697	(8.66	0.30	$0.29) \times 10^{-5}$	15.3 — 18.0	703	(1.95	0.07	$0.06) \times 10^{-4}$

Table 23: For Bartels Rotation 2552 to 2558 (Sep 06, 2020 – Feb 15, 2021), the observed antiproton numbers, antiproton to proton flux ratio and the respective statistical and systematic uncertainties.

Rigidity (GV)	$N_{\bar{p}}$	$\frac{\Phi_{\bar{p}}}{\Phi_p}$	σ_{stat}	σ_{syst}	Rigidity (GV)	$N_{\bar{p}}$	$\frac{\Phi_{\bar{p}}}{\Phi_p}$	σ_{stat}	σ_{syst}
1.16 — 1.51	21	(5.45	0.97	$0.50) \times 10^{-5}$	5.37 — 6.47	446	(1.22	0.05	$0.05) \times 10^{-4}$
1.51 — 1.92	22	(2.55	0.54	$0.23) \times 10^{-5}$	6.47 — 7.76	470	(1.40	0.06	$0.04) \times 10^{-4}$
1.92 — 2.40	42	(1.94	0.31	$0.16) \times 10^{-5}$	7.76 — 9.26	473	(1.62	0.07	$0.06) \times 10^{-4}$
2.40 — 2.97	139	(3.83	0.36	$0.19) \times 10^{-5}$	9.26 — 11.0	423	(1.61	0.07	$0.06) \times 10^{-4}$
2.97 — 3.64	245	(4.98	0.35	$0.26) \times 10^{-5}$	11.0 — 13.0	422	(1.89	0.08	$0.09) \times 10^{-4}$
3.64 — 4.43	288	(7.39	0.39	$0.31) \times 10^{-5}$	13.0 — 15.3	372	(1.96	0.09	$0.05) \times 10^{-4}$
4.43 — 5.37	321	(8.90	0.45	$0.39) \times 10^{-5}$	15.3 — 18.0	308	(1.87	0.10	$0.06) \times 10^{-4}$

Table 24: For Bartels Rotation 2558 to 2564 (Feb 15, 2021 – Jul 27, 2021), the observed antiproton numbers, antiproton to proton flux ratio and the respective statistical and systematic uncertainties.

BIBLIOGRAPHY

- [1] M. Aguilar et al. (AMS Collaboration). Antiproton Flux, Antiproton-to-Proton Flux Ratio, and Properties of Elementary Particle Fluxes in Primary Cosmic Rays Measured with the Alpha Magnetic Spectrometer on the International Space Station. *Phys. Rev. Lett.*, 117:091103, Aug 2016. DOI: [10.1103/PhysRevLett.117.091103](https://doi.org/10.1103/PhysRevLett.117.091103).
- [2] NobelPrize.org (Nobel Media AB). Victor F. Hess - Facts, 2022. URL: <https://www.nobelprize.org/prizes/physics/1936/hess/facts>.
- [3] C. D. Anderson. The Positive Electron. *Phys. Rev.*, 43:491–494, Mar 1933. DOI: [10.1103/PhysRev.43.491](https://doi.org/10.1103/PhysRev.43.491).
- [4] O. Chamberlain, E. Segre, and C. Wiegand. Antiprotons. *Technical Report*, Nov 1955. DOI: [10.2172/915070](https://doi.org/10.2172/915070).
- [5] E. A. Bogomolov, N. D. Lubyanaya, V. A. Romanov, S. V. Stepanov, and M. S. Shulakova. A Stratospheric Magnetic Spectrometer Investigation of the Singly Charged Component Spectra and Composition of the Primary and Secondary Cosmic Radiation. In *International Cosmic Ray Conference*, volume 1, page 330, 1979. URL: <https://articles.adsabs.harvard.edu/pdf/1979ICRC...16a.330B>.
- [6] R. L. Golden, S. Horan, B. G. Mauger, G. D. Badhwar, J. L. Lacy, S. A. Stephens, R. R. Daniel, and J. E. Zipse. Evidence for the Existence of Cosmic-Ray Antiprotons. *Phys. Rev. Lett.*, 43:1196–1199, Oct 1979. DOI: [10.1103/PhysRevLett.43.1196](https://doi.org/10.1103/PhysRevLett.43.1196).
- [7] O. Adriani et al. Measurement of the flux of primary cosmic ray antiprotons with energies of 60-MeV to 350-GeV in the PAMELA experiment. *JETP Letters*, 96:621–627, 2013. DOI: [10.1134/S002136401222002X](https://doi.org/10.1134/S002136401222002X).
- [8] K. Greisen. End to the Cosmic-Ray Spectrum? *Phys. Rev. Lett.*, 16:748–750, Apr 1966. DOI: [10.1103/PhysRevLett.16.748](https://doi.org/10.1103/PhysRevLett.16.748).
- [9] G. T. Zatsepin and V. A. Kuzmin. Upper Limit of the Spectrum of Cosmic Rays. *Soviet Journal of Experimental and Theoretical Physics Letters*, 4:78, Aug 1966. URL: <https://www.osti.gov/biblio/4515382>.
- [10] D. J. Bird et al. Detection of a Cosmic Ray with Measured Energy Well beyond the Expected Spectral Cutoff due to Cosmic Microwave Radiation. *Astrophysical Journal*, 441:144, Mar 1995. DOI: [10.1086/175344](https://doi.org/10.1086/175344).
- [11] R. Abbasi et al. Indications of Intermediate-Scale Anisotropy of Cosmic Rays with Energy Greater Than 57 EeV in the Northern Sky Measured with the Surface Detector of the Telescope Array Experiment. *The Astrophysical Journal*, 790(2):L21, Jul 2014. DOI: [10.1088/2041-8205/790/2/l21](https://doi.org/10.1088/2041-8205/790/2/l21).
- [12] A. Lopez-Oramas. Multi-year Campaign of the Gamma-Ray Binary LS I +61° 303 and Search for VHE Emission from Gamma-Ray Binary Candidates with the MAGIC Telescopes. PhD thesis, Universitat Autònoma de Barcelona, Apr 2015. DOI: [10.13140/RG.2.1.4140.4969](https://doi.org/10.13140/RG.2.1.4140.4969).
- [13] R. L. Workman et al. (Particle Data Group). Review of Particle Physics. *Prog. Theor. Exp. Phys.*, 2022:p.083C01, 2022. DOI: [10.1093/ptep/ptac097](https://doi.org/10.1093/ptep/ptac097).

- 1337 [14] A. Pacini. Cosmic rays: Bringing messages from the sky to the Earth's surface. *Revista*
 1338 *Brasileira de Ensino de Fisica*, 39, Jan 2017. DOI: [10.1590/1806-9126-RBEF-2016-0168](https://doi.org/10.1590/1806-9126-RBEF-2016-0168).
- 1339 [15] W. Baade and F. Zwicky. Cosmic Rays from Super-novae. *Proceedings of the Na-*
 1340 *tional Academy of Sciences of the United States of America*, 20(5):259–263, 1934. URL:
 1341 <http://www.jstor.org/stable/86841>.
- 1342 [16] M. Turatto. Classification of Supernovae, pages 21–36. Springer Berlin Heidelberg, Berlin,
 1343 Heidelberg, 2003. DOI: [10.1007/3-540-45863-8_3](https://doi.org/10.1007/3-540-45863-8_3).
- 1344 [17] S. P. Reynolds. Supernova Remnants at High Energy. *Annual Review of Astronomy and*
 1345 *Astrophysics*, 46(1):89–126, 2008. DOI: [10.1146/annurev.astro.46.060407.145237](https://doi.org/10.1146/annurev.astro.46.060407.145237).
- 1346 [18] M. S. Longair. High Energy Astrophysics. UK: Cambridge University Press, 2011. URL:
 1347 <https://ui.adsabs.harvard.edu/abs/2011hea..book....L>.
- 1348 [19] E. Fermi. On the Origin of the Cosmic Radiation. *Phys. Rev.*, 75:1169–1174, Apr 1949. DOI:
 1349 [10.1103/PhysRev.75.1169](https://doi.org/10.1103/PhysRev.75.1169).
- 1350 [20] T. Gold, F. G. Smith, and A. W. Wolfendale. Pulsars and the Origin of Cosmic Rays and
 1351 Discussion. *Philosophical Transactions of the Royal Society of London. Series A, Mathematical*
 1352 *and Physical Sciences*, 277(1270):453–461, 1975. URL: <http://www.jstor.org/stable/74493>.
- 1353 [21] W. Bednarek and M. Bartosik. Cosmic rays from Galactic pulsars. *Astronomy & Astrophysics*,
 1354 423(2):405–413, 2004. DOI: [10.1051/0004-6361:20047005](https://doi.org/10.1051/0004-6361:20047005).
- 1355 [22] J. Arons. Pulsar wind nebulae as cosmic pevatrons: A current sheet's tale. *Space Science*
 1356 *Reviews*, 173:341–367, 2012. DOI: [10.1007/s11214-012-9885-1](https://doi.org/10.1007/s11214-012-9885-1).
- 1357 [23] A. R. Bell. Cosmic ray acceleration in pulsar-driven supernova remnants. *Monthly Notices of*
 1358 *the Royal Astronomical Society*, 257(3):493–500, Aug 1992. DOI: [10.1093/mnras/257.3.493](https://doi.org/10.1093/mnras/257.3.493).
- 1359 [24] D. Hooper, P. Blasi, and P. D. Serpico. Pulsars as the sources of high energy cosmic ray
 1360 positrons. *Journal of Cosmology and Astroparticle Physics*, 2009(01):025, Jan 2009. DOI:
 1361 [10.1088/1475-7516/2009/01/025](https://doi.org/10.1088/1475-7516/2009/01/025).
- 1362 [25] R. Cowsik. Positrons and Antiprotons in Galactic Cosmic Rays. *Annual Review of Nuclear*
 1363 *and Particle Science*, 66(1):297–319, 2016. DOI: [10.1146/annurev-nucl-102115-044851](https://doi.org/10.1146/annurev-nucl-102115-044851).
- 1364 [26] V. Bresci, E. Amato, P. Blasi, and G. Morlino. Effects of re-acceleration and source gram-
 1365 mage on secondary cosmic rays spectra. *Monthly Notices of the Royal Astronomical Society*,
 1366 488(2):2068–2078, 07 2019. DOI: [10.1093/mnras/stz1806](https://doi.org/10.1093/mnras/stz1806).
- 1367 [27] I. Cholis, T. Linden, and D. Hooper. A robust excess in the cosmic-ray antiproton spec-
 1368 trum: Implications for annihilating dark matter. *Phys. Rev. D*, 99:103026, May 2019. DOI:
 1369 [10.1103/PhysRevD.99.103026](https://doi.org/10.1103/PhysRevD.99.103026).
- 1370 [28] J. Heisig. Cosmic-ray antiprotons in the AMS-02 era: A sensitive probe of dark matter. *Modern*
 1371 *Physics Letters A*, 36(05):2130003, 2021. DOI: [10.1142/S0217732321300032](https://doi.org/10.1142/S0217732321300032).
- 1372 [29] M. W. Winkler. Cosmic ray antiprotons at high energies. *Journal of Cosmology and Astropar-*

- 1373 *ticle Physics*, 2017(02):048, Feb 2017. DOI: [10.1088/1475-7516/2017/02/048](https://doi.org/10.1088/1475-7516/2017/02/048).
- 1374 [30] R. Kappl and M. W. Winkler. The cosmic ray antiproton background for AMS-02. *Journal*
1375 *of Cosmology and Astroparticle Physics*, 2014(09):051–051, Sep 2014. DOI: [10.1088/1475-7516/2014/09/051](https://doi.org/10.1088/1475-7516/2014/09/051).
- 1377 [31] M. Cui, Q. Yuan, Y. Tsai, and Y. Fan. Possible dark matter annihilation signal in the
1378 ams-02 antiproton data. *Phys. Rev. Lett.*, 118:191101, May 2017. DOI: [10.1103/PhysRevLett.118.191101](https://doi.org/10.1103/PhysRevLett.118.191101).
- 1380 [32] A. W. Strong, I. V. Moskalenko, and V. S. Ptuskin. Cosmic-Ray Propagation and Interactions
1381 in the Galaxy. *Annual Review of Nuclear and Particle Science*, 57(1):285–327, 2007. DOI:
1382 [10.1146/annurev.nucl.57.090506.123011](https://doi.org/10.1146/annurev.nucl.57.090506.123011).
- 1383 [33] I. V. Moskalenko. Galprop: modeling cosmic ray propagation and associated interstellar emis-
1384 sions, 2011. DOI: [10.48550/ARXIV.1105.4921](https://doi.org/10.48550/ARXIV.1105.4921).
- 1385 [34] D. Maurin. USINE: Semi-analytical models for Galactic cosmic-ray propagation. *Computer*
1386 *Physics Communications*, 247:106942, 2020. DOI: [10.1016/j.cpc.2019.106942](https://doi.org/10.1016/j.cpc.2019.106942).
- 1387 [35] C. Evoli et al. Cosmic-ray propagation with DRAGON2: I. numerical solver and astrophysical
1388 ingredients. *Journal of Cosmology and Astroparticle Physics*, 2017(02):015–015, Feb 2017.
1389 DOI: [10.1088/1475-7516/2017/02/015](https://doi.org/10.1088/1475-7516/2017/02/015).
- 1390 [36] V. S. Ptuskin, O. N. Strelnikova, and L. G. Sveshnikova. On leaky-box approximation to GAL-
1391 PROP. *Astroparticle Physics*, 31:284–289, 2009. DOI: [10.1016/j.astropartphys.2009.02.004](https://doi.org/10.1016/j.astropartphys.2009.02.004).
- 1392 [37] E. N. Parker. Dynamics of the Interplanetary Gas and Magnetic Fields. *Astrophysical Journal*,
1393 128:664, Nov 1958. DOI: [10.1086/146579](https://doi.org/10.1086/146579).
- 1394 [38] C. T. Russell. The Solar Wind and Magnetospheric Dynamics. In *Correlated Interplanetary*
1395 *and Magnetospheric Observations*, pages 3–47. Springer Netherlands, 1974. DOI: [10.1007/978-94-010-2172-2_1](https://doi.org/10.1007/978-94-010-2172-2_1).
- 1397 [39] M. J. Owens and R. J. Forsyth. The Heliospheric Magnetic Field. *Living Reviews in Solar*
1398 *Physics*, 10, Nov 2013. DOI: [10.12942/lrsp-2013-5](https://doi.org/10.12942/lrsp-2013-5).
- 1399 [40] A. J. Dessler. Solar wind and interplanetary magnetic field. *Reviews of Geophysics*, 5(1):1–41,
1400 1967. DOI: [10.1029/RG005i001p00001](https://doi.org/10.1029/RG005i001p00001).
- 1401 [41] R. Cowen. Voyager 1 has reached interstellar space. *Nature*, 2013. DOI: [10.1038/nature.2013.13735](https://doi.org/10.1038/nature.2013.13735).
- 1403 [42] NASA. Solar wind at voyager 1, 2012. Retrieved 16:20, July 20, 2022 from: https://commons.wikimedia.org/wiki/File:Solar_wind_at_Voyager_1.png.
- 1405 [43] D. H. Hathaway. The Solar Cycle. *Living Reviews in Solar Physics*, 7(1):1, Dec 2010. DOI:
1406 [10.12942/lrsp-2010-1](https://doi.org/10.12942/lrsp-2010-1).
- 1407 [44] C. Jorgensen et al. Christian Horrebow’s Sunspot Observations – I. Life and Published Writ-
1408 ings. *Solar Physics*, 294:77, Jun 2019. DOI: [10.1007/s11207-019-1465-z](https://doi.org/10.1007/s11207-019-1465-z).

- 1409** [45] K. Christoffer et al. Christian Horrebow's Sunspot Observations – II. Construction of a Record
1410 of Sunspot Positions. *Solar Physics*, 294:78, Jun 2019. DOI: [10.1007/s11207-019-1466-y](https://doi.org/10.1007/s11207-019-1466-y).
- 1411** [46] L. Gleeson and W. Axford. Solar Modulation of Galactic Cosmic Rays. *Astrophysical Journal*,
1412 154:1011, Dec 1968. DOI: [10.1086/149822](https://doi.org/10.1086/149822).
- 1413** [47] E. Ross and W. J. Chaplin. The behaviour of galactic cosmic ray intensity during solar activity
1414 cycle 24. *Solar Physics*, 294(1):8, Jan 2019. DOI: [10.1007/s11207-019-1397-7](https://doi.org/10.1007/s11207-019-1397-7).
- 1415** [48] M. Aguilar et al. (AMS Collaboration). Observation of complex time structures in the cosmic-ray
1416 electron and positron fluxes with the alpha magnetic spectrometer on the international
1417 space station. *Phys. Rev. Lett.*, 121:051102, Jul 2018. DOI: [10.1103/PhysRevLett.121.051102](https://doi.org/10.1103/PhysRevLett.121.051102).
- 1418** [49] NobelPrize.org (Nobel Media AB). The Nobel Prize in Physics 1959, 2022. URL: <https://www.nobelprize.org/prizes/physics/1959/summary>.
- 1420** [50] K. Anraku et al. (BESS Collaboration). Balloon borne experiment using a superconducting
1421 solenoidal magnet spectrometer. In *KEK-PREPRINT-94-40*, 6 1994. URL: <https://lib-extopc.kek.jp/preprints/PDF/1994/9427/9427040.pdf>.
- 1423** [51] M. Nozaki for the BESS-Polar Collaboration. BESS-Polar. *Nuclear Instruments and Methods
 in Physics Research Section B: Beam Interactions with Materials and Atoms*, 214:110–115,
1424 2004. DOI: [10.1016/j.nimb.2003.08.005](https://doi.org/10.1016/j.nimb.2003.08.005).
- 1426** [52] T. Yoshida et al. Bess-polar experiment. *Life sciences and space research*, 33(10):1755–1762,
1427 2004. DOI: [10.1016/j.asr.2003.05.017](https://doi.org/10.1016/j.asr.2003.05.017).
- 1428** [53] K. Abe et al. (BESS Collaboration). Measurement of the cosmic-ray low-energy antiproton
1429 spectrum with the first BESS-Polar Antarctic flight. *Physics Letters B*, 670(2):103–108, 2008.
1430 DOI: [10.1016/j.physletb.2008.10.053](https://doi.org/10.1016/j.physletb.2008.10.053).
- 1431** [54] K. Abe et al. Measurement of the Cosmic-Ray Antiproton Spectrum at Solar Minimum with a
1432 Long-Duration Balloon Flight over Antarctica. *Phys. Rev. Lett.*, 108:051102, Jan 2012. DOI:
1433 [10.1103/PhysRevLett.108.051102](https://doi.org/10.1103/PhysRevLett.108.051102).
- 1434** [55] A. M. Galper et al. The PAMELA experiment: a decade of Cosmic Ray Physics in
1435 space. *Journal of Physics: Conference Series*, 798:012033, Jan 2017. DOI: [10.1088/1742-6596/798/1/012033](https://doi.org/10.1088/1742-6596/798/1/012033).
- 1437** [56] O. Adriani et al. (PAMELA Collaboration). New Measurement of the Antiproton-to-Proton
1438 Flux Ratio up to 100 GeV in the Cosmic Radiation. *Phys. Rev. Lett.*, 102:051101, Feb 2009.
1439 DOI: [10.1103/PhysRevLett.102.051101](https://doi.org/10.1103/PhysRevLett.102.051101).
- 1440** [57] O. Adriani et al. (PAMELA Collaboration). PAMELA Results on the Cosmic-Ray Antiproton
1441 Flux from 60 MeV to 180 GeV in Kinetic Energy. *Phys. Rev. Lett.*, 105:121101, Sep 2010.
1442 DOI: [10.1103/PhysRevLett.105.121101](https://doi.org/10.1103/PhysRevLett.105.121101).
- 1443** [58] S. Haino et al. Measurement of cosmic-ray antiproton spectrum with BESS-2002.
1444 In *29th International Cosmic Ray Conference*, volume 3, page 13, Jan 2005. URL:
1445 <https://ui.adsabs.harvard.edu/abs/2005ICRC....3...13H>.

- 1446** [59] Y. Asaoka et al. Measurements of Cosmic-Ray Low-Energy Antiproton and Proton Spectra
1447 in a Transient Period of Solar Field Reversal. *PhysRevLett*, 88(5):051101, Feb 2002. DOI:
1448 [10.1103/PhysRevLett.88.051101](https://doi.org/10.1103/PhysRevLett.88.051101).
- 1449** [60] A. Moiseev et al. Cosmic-Ray Antiproton Flux in the Energy Range from 200 to 600 MeV.
1450 *The Astrophysical Journal*, 474(1):479–489, Jan 1997. DOI: [10.1086/303463](https://doi.org/10.1086/303463).
- 1451** [61] H. Matsunaga et al. Measurement of Low-Energy Cosmic-Ray Antiprotons at Solar Minimum.
1452 *PhysRevLett*, 81(19):4052–4055, Nov 1998. DOI: [10.1103/PhysRevLett.81.4052](https://doi.org/10.1103/PhysRevLett.81.4052).
- 1453** [62] S. Orito et al. Precision Measurement of Cosmic-Ray Antiproton Spectrum. *PhysRevLett*,
1454 84(6):1078–1081, Feb 2000. DOI: [10.1103/PhysRevLett.84.1078](https://doi.org/10.1103/PhysRevLett.84.1078).
- 1455** [63] T. Maeno et al. Successive measurements of cosmic-ray antiproton spectrum in a positive
1456 phase of the solar cycle. *Astroparticle Physics*, 16(2):121–128, Nov 2001. DOI: [10.1016/S0927-6505\(01\)00107-4](https://doi.org/10.1016/S0927-6505(01)00107-4).
- 1458** [64] M. Boezio et al. The Cosmic-Ray Antiproton Flux between 0.62 and 3.19 GeV Measured
1459 Near Solar Minimum Activity. *The Astrophysical Journal*, 487(1):415–423, Sep 1997. DOI:
1460 [10.1086/304593](https://doi.org/10.1086/304593).
- 1461** [65] M. Boezio et al. The Cosmic-Ray Antiproton Flux between 3 and 49 GeV. *The Astrophysical
1462 Journal*, 561(2):787–799, Nov 2001. DOI: [10.1086/323366](https://doi.org/10.1086/323366).
- 1463** [66] J. Mitchell et al. Measurement of 0.25-3.2 GeV Antiprotons in the Cosmic Radiation. *Phys-
1464 RevLett*, 76(17):3057–3060, Apr 1996. DOI: [10.1103/PhysRevLett.76.3057](https://doi.org/10.1103/PhysRevLett.76.3057).
- 1465** [67] G. Basini. The Flux of Cosmic Ray Antiprotons from 3.7 to 24 GeV. In
1466 *26th International Cosmic Ray Conference*, volume 3, page 77, Aug 1999. URL:
1467 <https://ui.adsabs.harvard.edu/abs/1999ICRC....3....77B>.
- 1468** [68] M. Aguilar et al. (AMS Collaboration). Precision Measurement of the Proton Flux in Primary
1469 Cosmic Rays from Rigidity 1 GV to 1.8 TV with the Alpha Magnetic Spectrometer on the
1470 International Space Station. *Phys. Rev. Lett.*, 114:171103, Apr 2015. DOI: [10.1103/Phys-RevLett.114.171103](https://doi.org/10.1103/Phys-RevLett.114.171103).
- 1472** [69] Q. An et al. Measurement of the cosmic-ray proton spectrum from 40 GeV to 100 TeV with
1473 the DAMPE satellite. *Science Advances*, 5(9):eaax3793, 2019. DOI: [10.1126/sciadv.aax3793](https://doi.org/10.1126/sciadv.aax3793).
- 1474** [70] O. Adriani et al. PAMELA Measurements of Cosmic-Ray Proton and Helium Spectra. *Science*,
1475 332(6025):69–72, 2011. DOI: [10.1126/science.1199172](https://doi.org/10.1126/science.1199172).
- 1476** [71] A. D. Panov et al. Energy Spectra of Abundant Nuclei of Primary Cosmic Rays from the Data
1477 of ATIC-2 Experiment: Final Results. *Bulletin of the Russian Academy of Sciences: Physics*,
1478 73(5):564–567, 2009. DOI: [10.3103/S1062873809050098](https://doi.org/10.3103/S1062873809050098).
- 1479** [72] Y. S. Yoon et al. Proton and Helium Spectra from the CREAM-III Flight. *The Astrophysical
1480 Journal*, 839(1):5, 2017. DOI: [10.3847/1538-4357/aa68e4](https://doi.org/10.3847/1538-4357/aa68e4).
- 1481** [73] E. Atkin et al. New Universal Cosmic-Ray Knee near a Magnetic Rigidity of 10 TV with the
1482 NUCLEON Space Observatory. *Jetp Lett*, 108:5–12, 2018. DOI: [10.1134/S0021364018130015](https://doi.org/10.1134/S0021364018130015).

- 1483 [74] S. Ahlen et al. An antimatter spectrometer in space. *Nuclear Instruments and Methods in*
 1484 *Physics Research Section A: Accelerators, Spectrometers, Detectors and Associated Equipment*,
 1485 350(1):351–367, 1994. DOI: [10.1016/0168-9002\(94\)91184-3](https://doi.org/10.1016/0168-9002(94)91184-3).
- 1486 [75] R. Battiston. The antimatter spectrometer (AMS-02): A particle physics detector in space.
 1487 *Nuclear Instruments and Methods in Physics Research Section A: Accelerators, Spectrometers,*
 1488 *Detectors and Associated Equipment*, 588(1):227–234, 2008. DOI: [10.1016/j.nima.2008.01.044](https://doi.org/10.1016/j.nima.2008.01.044).
- 1489 [76] M. Aguilar et al. (AMS Collaboration). The Alpha Magnetic Spectrometer (AMS) on the
 1490 International Space Station: Part I - results from the test flight on the space shuttle. *Physics*
 1491 *Reports*, 366(6):331–405, 2002. DOI: [10.1016/S0370-1573\(02\)00013-3](https://doi.org/10.1016/S0370-1573(02)00013-3).
- 1492 [77] Roskosmos. STS-91 PLB, 1998. Retrieved 16:20, July 20, 2022 from: https://commons.wikimedia.org/wiki/File:STS-91_PLB.jpg.
- 1493 [78] AMS-01 Collaboration. AMS-01 Brochure. URL: <https://ams.cern.ch/ams01/5.htm>.
- 1494 [79] NASA/Crew-2. View of the ISS taken during crew-2 flyaround (iss066-e-081311), 2021.
 1495 Retrieved 16:20, July 20, 2022 from: [https://commons.wikimedia.org/wiki/File:View_of_the_ISS_taken_during_Crew-2_flyaround_\(ISS066-E-081311\).jpg](https://commons.wikimedia.org/wiki/File:View_of_the_ISS_taken_during_Crew-2_flyaround_(ISS066-E-081311).jpg).
- 1496 [80] M. Aguilar et al. (AMS Collaboration). The Alpha Magnetic Spectrometer (AMS) on the
 1497 international space station: Part II – Results from the first seven years. *Physics Reports*,
 1500 894:1–116, 2021. DOI: [10.1016/j.physrep.2020.09.003](https://doi.org/10.1016/j.physrep.2020.09.003).
- 1501 [81] F. Machate. *Study for large acceptance electron analysis with the Alpha Magnetic Spectrometer*
 1502 *on the International Space Station*. Dissertation, RWTH Aachen University, Aachen, 2021.
 1503 DOI: [10.18154/RWTH-2021-09976](https://doi.org/10.18154/RWTH-2021-09976).
- 1504 [82] V. L. Ginzburg and I. M. Frank. Radiation of a Uniformly Moving Electron Due to Its
 1505 Transition from One Medium to Another. *J. Phys. (USSR)*, 9:353–362, 1945.
- 1506 [83] M. Heil et al. Operations and Alignment of the AMS-02 Transition Radiation Detector.
 1507 In *33rd International Cosmic Ray Conference*, page 1232, 2013. URL:
 1508 <https://www.cbpf.br/icrc2013/papers/icrc2013-1232.pdf>.
- 1509 [84] T. Siedenburg. The AMS TRD. A gasdetector designed for operation in space. *Nuclear Physics*
 1510 *B - Proceedings Supplements*, 150:30–33, 2006. DOI: [10.1016/j.nuclphysbps.2004.06.001](https://doi.org/10.1016/j.nuclphysbps.2004.06.001).
- 1511 [85] AMS Collaboration. The Alpha Magnetic Spectrometer on the International Space Station,
 1512 2022. URL: <https://ams02.space>.
- 1513 [86] P. E. Saouter. Operation and Performance of AMS-02 Silicon Tracker. *PoS*, Vertex2014:028,
 1514 2015. DOI: [10.22323/1.227.0028](https://doi.org/10.22323/1.227.0028).
- 1515 [87] S. Haino. Performance of the AMS-02 silicon tracker in the ISS mission. *Nuclear Instruments*
 1516 *and Methods in Physics Research Section A: Accelerators, Spectrometers, Detectors and*
 1517 *Associated Equipment*, 699:221–224, 2013. DOI: [10.1016/j.nima.2012.05.060](https://doi.org/10.1016/j.nima.2012.05.060).
- 1518 [88] D. Haas. The Silicon Tracker of AMS02. *Nuclear Instruments and Methods in Physics Research*
 1519 *Section A: Accelerators, Spectrometers, Detectors and Associated Equipment*, 530(1):173–177,

- 1520 2004. DOI: [10.1016/j.nima.2004.05.068](https://doi.org/10.1016/j.nima.2004.05.068).
- 1521 [89] G. Ambrosi et al. Alignment of the AMS-02 Silicon Tracker. In *33rd International Cosmic Ray Conference*, page 1260, 2013. URL: <https://ui.adsabs.harvard.edu/abs/2013ICRC...33..570A>.
- 1522
- 1523 [90] B. Alpat et al. The internal alignment and position resolution of the ams-02 silicon tracker
1524 determined with cosmic-ray muons. *Nuclear Instruments and Methods in Physics Research*
1525 *Section A: Accelerators, Spectrometers, Detectors and Associated Equipment*, 613(2):207–217,
1526 2010. DOI: [10.1016/j.nima.2009.11.065](https://doi.org/10.1016/j.nima.2009.11.065).
- 1527 [91] R. L. Gluckstern. Uncertainties in track momentum and direction, due to multiple scattering
1528 and measurement errors. *Nuclear Instruments and Methods*, 24:381–389, Jul 1963. DOI:
1529 [10.1016/0029-554X\(63\)90347-1](https://doi.org/10.1016/0029-554X(63)90347-1).
- 1530 [92] P. Zuccon. AMS-02 Track reconstruction and rigidity measurement. In *33rd Interna-*
1531 *tional Cosmic Ray Conference*, page 1064, 2013. URL: <https://s3.cern.ch/inspire-prod-files-7/71c48c76263c1f7bee2621c779ba3320>.
- 1532
- 1533 [93] V. Bindi et al. Calibration and performance of the AMS-02 time of flight detector in space.
1534 *Nuclear Instruments and Methods in Physics Research Section A: Accelerators, Spectrometers,*
1535 *Detectors and Associated Equipment*, 743:22–29, 2014. DOI: [10.1016/j.nima.2014.01.002](https://doi.org/10.1016/j.nima.2014.01.002).
- 1536 [94] V. Bindi et al. The time of flight detector of the AMS-02 experiment on the interna-
1537 tional space station. *Nuclear Instruments and Methods in Physics Research Section A: Ac-*
1538 *celerators, Spectrometers, Detectors and Associated Equipment*, 718:478–480, 2013. DOI:
1539 [10.1016/j.nima.2012.11.061](https://doi.org/10.1016/j.nima.2012.11.061).
- 1540 [95] V. Bindi et al. The AMS-02 Time of Flight (TOF) System: Construction and Overall Perfor-
1541 mances in Space. In *International Cosmic Ray Conference*, volume 33, page 2298, Jan 2013.
1542 URL: <https://ui.adsabs.harvard.edu/abs/2013ICRC...33.2298B>.
- 1543 [96] L. Hu et al. The RICH detector of AMS-02: 5 years of operation in space. *Nuclear Instru-*
1544 *ments and Methods in Physics Research Section A: Accelerators, Spectrometers, Detectors and*
1545 *Associated Equipment*, 876:5–8, 2017. DOI: [10.1016/j.nima.2016.12.011](https://doi.org/10.1016/j.nima.2016.12.011).
- 1546 [97] R. Pereira. The AMS-02 RICH detector: Performance during ground-based data tak-
1547 ing at CERN. *Nuclear Instruments and Methods in Physics Research Section A: Ac-*
1548 *celerators, Spectrometers, Detectors and Associated Equipment*, 639:37–41, 2011. DOI:
1549 [10.1016/j.nima.2010.09.036](https://doi.org/10.1016/j.nima.2010.09.036).
- 1550 [98] F. Giovacchini, J. Casaus, and A. Oliva. The AMS-02 RICH detector: Status and
1551 physics results. *Nuclear Instruments and Methods in Physics Research Section A: Ac-*
1552 *celerators, Spectrometers, Detectors and Associated Equipment*, 952:161797, 2020. DOI:
1553 [10.1016/j.nima.2019.01.024](https://doi.org/10.1016/j.nima.2019.01.024).
- 1554 [99] F. Giovacchini. Performance in space of the AMS-02 RICH detector. *Nuclear Instruments and*
1555 *Methods in Physics Research Section A: Accelerators, Spectrometers, Detectors and Associated*
1556 *Equipment*, 766:57–60, 2014. DOI: [10.1016/j.nima.2014.04.036](https://doi.org/10.1016/j.nima.2014.04.036).
- 1557 [100] R. L. Sylvie. Performance of the AMS02 electromagnetic calorimeter in space. *Journal of*
1558 *Physics: Conference Series*, 404:012034, 2012. DOI: [10.1088/1742-6596/404/1/012034](https://doi.org/10.1088/1742-6596/404/1/012034).

- 1559** [101] M. Vecchi et al. The electromagnetic calorimeter of the AMS-02 experiment. In *Semaine de l’Astrophysique Francaise (SF2A 2012)*, Nice, France, Jun 2012. URL: <http://hal.in2p3.fr/in2p3-00745677>.
- 1560**
- 1562** [102] C. Adloff et al. The AMS-02 lead-scintillating fibres Electromagnetic Calorimeter. *Nuclear Instruments and Methods in Physics Research Section A: Accelerators, Spectrometers, Detectors and Associated Equipment*, 714:147–154, 2013. DOI: [10.1016/j.nima.2013.02.020](https://doi.org/10.1016/j.nima.2013.02.020).
- 1563**
- 1565** [103] I. Marco. Performance of the AMS-02 Electromagnetic Calorimeter in Space. *PoS*, TIPP2014:025, 2014. DOI: [10.22323/1.213.0025](https://doi.org/10.22323/1.213.0025).
- 1566**
- 1567** [104] M. Vecchi, K. Wu, and Y. Chang. A 3-dimensional electromagnetic shower characterization and its application to AMS-02 pointing capability. In *33rd International Cosmic Ray Conference*, page 0653, 2013.
- 1569**
- 1570** [105] D. F. Stefano. Results of 2007 test beam of AMS-02 Electromagnetic Calorimeter. *Advances in Space Research*, 45:112–122, 2010. DOI: [10.1016/j.asr.2009.08.005](https://doi.org/10.1016/j.asr.2009.08.005).
- 1571**
- 1572** [106] G. Gallucci and (for the AMS-02 ECAL group). Performance of the AMS-02 Electromagnetic Calorimeter in Space. *Journal of Physics: Conference Series*, 587:012028, Feb 2015. DOI: [10.1088/1742-6596/587/1/012028](https://doi.org/10.1088/1742-6596/587/1/012028).
- 1573**
- 1575** [107] P. von Doetinchem et al. The AMS-02 Anticoincidence Counter. *Nuclear Physics B - Proceedings Supplements*, 197:15–18, 2009. DOI: [10.1016/j.nuclphysbps.2009.10.025](https://doi.org/10.1016/j.nuclphysbps.2009.10.025).
- 1576**
- 1577** [108] T. Bruch and W. Wallraff. The Anti-Coincidence Counter shield of the AMS tracker. *Nuclear Instruments and Methods in Physics Research Section A: Accelerators, Spectrometers, Detectors and Associated Equipment*, 572:505–507, 2007. DOI: [10.1016/j.nima.2006.10.376](https://doi.org/10.1016/j.nima.2006.10.376).
- 1579**
- 1580** [109] A. Basili et al. The TOF-ACC flight electronics for the fast trigger and time of flight of the AMS-02 cosmic ray spectrometer. *Nuclear Instruments and Methods in Physics Research Section A: Accelerators, Spectrometers, Detectors and Associated Equipment*, 707:99–113, 2013. DOI: [10.1016/j.nima.2012.12.089](https://doi.org/10.1016/j.nima.2012.12.089).
- 1581**
- 1584** [110] P. von Doetinchem et al. The Anticoincidence Counter System of AMS-02. In *International Cosmic Ray Conference*, Jun 2009. URL: <https://srl.utu.fi/AuxDOC/kocharov/ICRC2009/pdf/icrc1064.pdf>.
- 1585**
- 1587** [111] R. Brun and F. Rademakers. Root - An object oriented data analysis framework. *Nuclear Instruments and Methods in Physics Research Section A: Accelerators, Spectrometers, Detectors and Associated Equipment*, 389(1):81–86, 1997. DOI: [10.1016/S0168-9002\(97\)00048-X](https://doi.org/10.1016/S0168-9002(97)00048-X).
- 1588**
- 1590** [112] B. Beischer. *Measurement of high energy gamma rays from 200 MeV to 1 TeV with the Alpha Magnetic Spectrometer on the International Space Station*. Dissertation, RWTH Aachen University, Aachen, 2020. DOI: [10.18154/RWTH-2020-06535](https://doi.org/10.18154/RWTH-2020-06535).
- 1591**
- 1593** [113] J. Bartels. Twenty-seven day recurrences in terrestrial-magnetic and solar activity, 1923–1933. *Terrestrial Magnetism and Atmospheric Electricity*, 39(3):201–202a, 1934. DOI: [10.1029/TE039i003p00201](https://doi.org/10.1029/TE039i003p00201).
- 1594**
- 1596** [114] S. Agostinelli et al. GEANT4—a simulation toolkit. *Nuclear Instruments and Methods in*

- 1597** *Physics Research Section A: Accelerators, Spectrometers, Detectors and Associated Equipment*,
1598 506:250–303, 2003. DOI: [10.1016/S0168-9002\(03\)01368-8](https://doi.org/10.1016/S0168-9002(03)01368-8).
- 1599** [115] J. Allison et al. Recent developments in geant4. *Nuclear Instruments and Methods in Physics Research Section A: Accelerators, Spectrometers, Detectors and Associated Equipment*,
1600 835:186–225, 2016. DOI: [10.1016/j.nima.2016.06.125](https://doi.org/10.1016/j.nima.2016.06.125).
- 1602** [116] V. Helge et al. TMVA, the toolkit for multivariate data analysis with ROOT. In XI International Workshop on Advanced Computing and Analysis Techniques in Physics Research,
1603 volume 50, page 040. SISSA Medialab, 2009. DOI: [10.22323/1.050.0040](https://doi.org/10.22323/1.050.0040).
- 1605** [117] J. Neyman, E. S. Pearson, and K. Pearson. Ix. On the problem of the most efficient tests
1606 of statistical hypotheses. *Philosophical Transactions of the Royal Society of London. Series*
1607 *A, Containing Papers of a Mathematical or Physical Character*, 231(694-706):289–337, 1933.
1608 DOI: [10.1098/rsta.1933.0009](https://doi.org/10.1098/rsta.1933.0009).
- 1609** [118] J. D. Sullivan. Geometric factor and directional response of single and multi-element particle telescopes. *Nuclear Instruments and Methods*, 95(1):5–11, 1971. DOI: [10.1016/0029-554X\(71\)90033-4](https://doi.org/10.1016/0029-554X(71)90033-4).
- 1612** [119] N. Zimmermann. *Precision measurement of the cosmic-ray electron and positron fluxes as a function of time and energy with the Alpha Magnetic Spectrometer on the International Space Station*. Dissertation, RWTH Aachen University, Aachen, 2020. DOI: [10.18154/RWTH-2020-02650](https://doi.org/10.18154/RWTH-2020-02650).
- 1616** [120] C. Stormer. The polar aurora. *Quarterly Journal of the Royal Meteorological Society*,
1617 82(351):115–115, 1956. DOI: [10.1002/qj.49708235123](https://doi.org/10.1002/qj.49708235123).
- 1618** [121] G. D'Agostini. A multidimensional unfolding method based on Bayes' theorem. *Nuclear Instruments and Methods in Physics Research Section A: Accelerators, Spectrometers, Detectors and Associated Equipment*, 362(2):487–498, 1995. DOI: [10.1016/0168-9002\(95\)00274-X](https://doi.org/10.1016/0168-9002(95)00274-X).
- 1621** [122] T. Adye. Unfolding algorithms and tests using RooUnfold. In *PHYSTAT 2011*, pages 313–318,
1622 Geneva, 2011. CERN. DOI: [10.5170/CERN-2011-006.313](https://doi.org/10.5170/CERN-2011-006.313).
- 1623** [123] J. W. Bieber et al. Antiprotons at solar maximum. *Phys. Rev. Lett.*, 83:674–677, Jul 1999.
1624 DOI: [10.1103/PhysRevLett.83.674](https://doi.org/10.1103/PhysRevLett.83.674).
- 1625** [124] M. S. Potgieter et al. A perspective on the solar modulation of cosmic anti-matter. *Physics*,
1626 3(4):1190–1225, 2021. DOI: [10.3390/physics3040076](https://doi.org/10.3390/physics3040076).
- 1627** [125] S. Schael et al. AMS-100: The next generation magnetic spectrometer in space - An international science platform for physics and astrophysics at Lagrange point 2. *Nuclear Instruments and Methods in Physics Research Section A: Accelerators, Spectrometers, Detectors and Associated Equipment*, 944:162561, 2019. DOI: [10.1016/j.nima.2019.162561](https://doi.org/10.1016/j.nima.2019.162561).